CHALMERS

Simulation accuracy of the unsteady flow past slender cylinders

Evaluation and improvement of under hood simulation accuracy

Master's thesis in Applied Mechanics

HANNES WÄSTLUND

Department of Mechanics and Maritime Sciences
CHALMERS UNIVERSITY OF TECHNOLOGY
Göteborg, Sweden 2018

MASTER'S THESIS IN APPLIED MECHANICS

Simulation accuracy of the unsteady flow past slender cylinders

Evaluation and improvement of under
hood simulation accuracy

HANNES WÄSTLUND

Department of Mechanics and Maritime Sciences
Division of Fluid Dynamics
CHALMERS UNIVERSITY OF TECHNOLOGY

Göteborg, Sweden 2018

Simulation accuracy of the unsteady flow past slender cylinders
Evaluation and improvement of under
hood simulation accuracy
HANNES WÄSTLUND

Master's thesis 2018:44
Department of Mechanics and Maritime Sciences
Division of Fluid Dynamics
Chalmers University of Technology
SE-412 96 Göteborg
Sweden
Telephone: +46 (0)31-772 1000

Chalmers Reproservice
Göteborg, Sweden 2018

Simulation accuracy of the unsteady flow past slender cylinders
Evaluation and improvement of under
hood simulation accuracy
Master's thesis in Applied Mechanics
HANNES WÄSTLUND
Department of Mechanics and Maritime Sciences
Division of Fluid Dynamics
Chalmers University of Technology

Abstract

The aim of the present study is to improve the accuracy of the predicted flow topology in the engine bays of cars when using both simple turbulence models based on the concept of Reynolds averaged Navier-Stokes (RANS) and more advanced models such as Detached Eddy Simulations (DES) and Large Eddy Simulations (LES). The focus has been to investigate the simple RANS models capability of predicting separation and the influence of unsteady wake movements (i.e vortex shedding) on the size of the created regions with recirculating flows and how much the accuracy can be improved by switching to the more advanced modelling approaches. In order to simplify the analysis of the studied models, they were tested on simple bluff bodies of cylindrical shape with different cross sections. The investigated geometries included polygonal shapes with 2, 4, 7, 8 and 16 sides and a circular cross section. The geometries were tested at different orientations and at a Reynolds number of $Re_d = 1 \cdot 10^4$, which is equivalent to that found for similar geometries in engine bays. The square cross section was also tested at a Reynolds number of $Re_d = 2.2 \cdot 10^4$. Both of these Reynolds numbers are below the critical number, which means that the boundary layers prior to separation is laminar. The behaviour of the different models have been compared to both experimental results, the LES results obtained in the present study and those from other numerical studies. The investigated RANS models included $k-\epsilon$ Realizable, $k-\omega$ SST, Reynolds Stress Model, $k-\epsilon$ $\overline{v_2'^2}f$ and Spalart-Allmaras.

An investigation of the development of the vortices and the transport of momentum into the base region predicted by eddy viscosity models, represented by $k-\omega$ SST, was performed for the square cross section. It was found that the initial creation of the vortices is fundamentally different than that found in experiments and by scale resolving methods. The actual creation of the vorticies takes place in the free shear layers after the separation points where small disturbances are amplified, turned into vortices and then enlarged by roll-up. For the eddy viscosity models, which are unable to resolve the roll-up process, the creation of the vortices are instead provided by separation at the trailing corner of the geometry. The modelled development of the vortex and the accumulation of mass and momentum into the vortices seems to be connected to their shape during the initial part of their existence, during which the vortices stick to the back side of the cylinder. The behaviour was found to be the result of a low pressure zone in the inner most part of the viscous sub-layer, which creates a force toward the surface of the cylinder. Further out in the buffer layer and the log-layer the force changes sign and is directed donwstream, partially due to the turbulent diffusion term. As a result an overestimation of the turbulence kinetic energy promotes the release of the vortices. The current flow contains many of the known weaknesses of the eddy viscosity approach, like a number of regions with stagnation flow and curved streamlines, which gives an overestimation of turbulent kinetic energy. The consequence is that the recirculation region lengths is underestimated by the eddy viscosity models due to increased transport of momentum into the wake. It is believed that this behaviour also influences the Strouhal number by increasing the vortex shedding frequency.

It was found that the eddy viscosity models are able to predict the vortex shedding process with an acceptable level of accuracy for polygonal shapes. However, the circular cross section constituted a bigger challenge. The recirculation region length was underestimated by approximately 30%. The separation was predicted to occur later than experiments performed by Bearman [2] and correlates with the expected separation behaviour at increased levels of turbulence. In order to get results of adequate accuracy for the separation point and recirculation region length, scale resolving approaches were needed.

Keywords: Engine bay, Vortex shedding, Flow topology, Separation, Reattachment, Bluff body, Computational Fluid Dynamics, Cylinder

Preface

The following thesis has been carried out between January and June 2018 as part of the authors education at the master program *Applied Mechanics* at *Chalmers University of Technology*, Gothenburg. The work has been carried out at the department *Cooling performance and heat treatment* at *Volvo Cars* under the supervision of Niklas Löfgren. Examiner for the thesis was prof. Lars Davidsson, at Chalmers University of Technology.

Acknowledgements

I would like to thank *Volvo Cars* for the opportunity to do my master thesis as part of their development process, as well as for all the resources made available during the thesis. I would also like to thank the staff at the department *Cooling performance and heat treatment*, and especially my supervisor Niklas Löfgren, for all the help and support during the execution of the thesis.

Nomenclature

α	Blending parameter
β_2	Model constant
β^*	Model constant
γ_2	Model constant
Δ	Grid filter width
Δx	Cell size ($V^{1/3}$)
δ	Surface cell thickness
δ_{ij}	Kronecker delta
ϵ	Dissipation rate
ϵ_0	Ambient dissipation rate
$\underline{\epsilon}, \underline{\epsilon}^h, \underline{\epsilon}^\omega$	Dissipation rate (RSM)
η	Model parameter
θ, θ_s	Angle/Separation angle
κ	von Kármán constant
μ, μ_t	Dynamic viscosity
ν	Kinematic viscosity
$\tilde{\nu}$	Modified diffusivity
ξ	Distance
ρ	Density
$\sigma_{k,\omega 1,\omega 2,\omega 3,\epsilon,\nu}$	Model constants
τ_w	Wall shear stress
τ_{ij}	Reynolds stresses
$\hat{\tau}_{ij}$	Sub-grid stresses
ϕ	Model parameter
$\underline{\phi}$,$\underline{\phi}^h$,$\underline{\phi}^\omega$	Pressure-strain
χ	Kinematic viscosity ratio
ω,$\tilde{\omega}$	Specific dissipation rate
ϑ	Turbulent velocity scale
ℓ	Turbulent length scale
A_c	Cylinder frontal area
A,$A_{0,s}$,a_1	Model coefficients
A_{ij}	Anisotropy tensor
B,B^{norm}	2-point correlations
C	Corner orientation
$C_{d/l}$	Coefficient of (drag/lift)
C_f	Skin friction coefficient
$C_{1,2,3,...}$	Model constants
$CD_{k\omega}$	Model parameter
D	Cylinder diameter
d	Distance to nearest wall
F	Face orientation
F_d	Drag force
$F_{1,2}$	Model parameters
f	Damping function
$f_{\nu 1,\nu 2,s,t2}$	Model parapeters

g	Model parameter
k	Turbulent kinetic energy
k_0	Ambient turbulent kinetic energy
L	Model parameter
l_R	Recirculation region length
l_t	Model parameter
l_W	Wake width in mean velocity field
N_{ij}	Model parameter
n	Wall normal vector
n_c	Number of cells per length scale
P, P_B	Pressures
$P^{k,\epsilon,f,\overline{v_2'^2}}$	Model production terms
Re_d	Reynolds number based on diameter
r	Radial coordinate
S	$\sqrt{2S_{ij}S_{ij}}$
S_{ij}	Strain rate tensor
St	Strouhal number
T_0	Corner at widest geometry point
T_1	Corner upstream of widest geometry point
t	Time
U_∞	Free stream velocity
u	Velocity vector
V	Cell volume
W	Model parameter
$\mathbf{X}, x, x_w, ...$	Position vectors,Distances
y^+	Normalised wall distance
$\mathbb{R}$	Rate of change term in momentum eq.
$\mathbb{C}$	Convection term in momentum eq.
$\mathbb{P}$	Pressure term in momentum eq.
$\mathbb{V}$	Viscous diffusion term in momentum eq.
$\mathbb{T}$	Turbulent diffusion term in momentum eq.
$\mathbb{M}$	Arbitrary term in momentum eq.
DES	Detached Eddy Simulations
LES	Large Eddy Simulations
$RANS, URANS$	Reynolds Averaged Navier-Stokes
RSM	Reynolds Stress Model
SST	Shear Stress Transport
$\overline{u}$	Time average of quantity
$\tilde{u}$	Periodic variation of quantity
u'	Random fluctuation of quantity
$\langle u \rangle$	Instantaneous mean of quantity ($\overline{u} + \tilde{u}$)
$\hat{u}$	Grid filtered quantity
$u_{t,o,r}$	Tangential, orthogonal and radial part

Contents

Abstract **i**

Preface **iii**

Acknowledgements **iii**

Nomenclature **v**

Contents **vii**

1 Background **1**
1.1 Previous studies . . . 1
1.2 Aim . . . 1
1.3 Specification of issue under investigation . . . 1
1.4 Limitations . . . 2
1.4.1 Ethical & ecological issues . . . 2

2 Theory **3**
2.1 Flow past slender cylinders . . . 3
2.2 Turbulence modelling . . . 4
2.2.1 Eddy viscosity models . . . 5
2.2.2 Reynolds Stress Model . . . 8
2.2.3 Smagorinsky model . . . 9
2.2.4 Detached Eddy Simulations . . . 10
2.3 Resolution of Scale Resolving Methods . . . 10

3 Method **11**
3.0.1 Computational domain & Mesh for RANS computations . . . 12
3.0.2 Computational domain & Mesh for scale resolving methods . . . 13
3.0.3 Numerical setup . . . 14
3.0.4 Boundary conditions . . . 14
3.0.5 Evaluation of resolution for scale resolving mesh . . . 15

4 Results **15**
4.0.1 Predictions of separation & reattachment . . . 16
4.0.2 Wake characteristics . . . 17
4.0.3 Vortex shedding process . . . 20
4.0.4 Momentum transport . . . 22
4.0.5 Summary of vortex development . . . 26
4.0.6 Further improvement . . . 29

5 Conclusion **34**
5.1 Future work . . . 35

References **36**

1 Background

The automotive industry rely heavily on physical testing when developing new designs. These methods have often been used for decades and are because of this both well tested and integrated into the work flow. Despite of this, physical experiments have some drawbacks when implemented as the main method of testing new concepts and designs. The test requires physical models which might be both expensive, difficult to manufacture and time demanding to prepare for testing. In some cases the geometry itself is an obstacle in the way that it does not permit experimental measurements to be performed without the flow being severely affected by the measurement equipment.

Numerical methods is an alternative to the physical tests and eliminates some of these drawbacks. It is cheaper and more time efficient since no physical models are needed. Because of the non-intrusive nature of numerical calculations it is also applicable in most flow cases. If the limitations of the used model is known, good understanding of the flow and reliable results can be obtained.

At Volvo cars the flow field and temperature distribution in the engine bay, referred to as aero-thermal conditions, are of great interest when determining the thermal loads and durability of different components. The implementation of physical tests inside the engine bay is however difficult to perform because of the high risk of affecting the flow field due to the limited space. Because of this, experimental data regarding the flow are non existent. Numerical methods are therefore of great interest.

1.1 Previous studies

The flow field in the engine bay can be computed with a high level of accuracy using Direct Numerical Simulation (DNS) or Large Eddy Simulation (LES). These methods are however very computationally demanding and are not suitable as the main method in product development. Because of this, simple and more time efficient methods, that have an acceptable level of accuracy, are needed. A steady state RANS solution, using k-ω SST, has been investigated in previous attempts by Menon [17] to develop such a method. In this study were both the flow through NACA ducts located on the under-body of the car and the flow created inside the engine bay by these ducts investigated. The function of the ducts is to provide streams of cooling air at specific components sensitive to thermal loads. It is because of this important to compute both the mass flow and the flow path accurately. Since no experimental results were available a reference solution was obtained using LES. The study concluded that parts of the flow field can be computed accurately under certain conditions. The flow through the ducts was computed with acceptable level of accuracy in therms of mass flow rate. However, the path of the flow was found to be more difficult to model. Especially for regions where the flow has to pass one or several components with complex geometry with separation and reattachment. A steady state RANS method was because of this found not to be applicable for computations of the complete engine bay.

1.2 Aim

The purpose of this paper is to improve both the knowledge about the aero-thermal conditions and the methods used for computing them within the engine bay. The improved methodology will enable Volvo Cars to develop and dimension new products with respect to their aero-thermal properties with a higher level of accuracy and as a result increase the durability and performance of their cars. The aim is to identify physical phenomenons and other factors inside the engine bay, which constitutes a challenge in therms of modelling accuracy and for numerical computation. This investigation will also conclude the accuracy and limitations for the different methods.

1.3 Specification of issue under investigation

The flow inside an engine bay is highly complex and previous attempts of finding critical regions and flow phenomena in terms of modelling accuracy has proved difficult. In order to simplify the process of finding the sources of the discrepancies, between simple RANS methods and the more accurate LES references, a simple academic case will be the foundation for this investigation. The use of a simple geometry gives a number of advantages. The first is, as already mentioned, that the flow phenomena under investigation can be isolated, which makes it easier to find both the source of the modelling challenge and how big impact modelling

errors and improvements have on the flow in close proximity of the object. Another advantage is that both experimental and numerical results will be available in the literature. In that way, both the simplified methods and the LES reference are validated further.

When the limitations and requirements for modelling the flow phenomena has been established the improvements can be implemented in a more complex engine bay flow situation. This will validate that the improved methodology gives the anticipated result even with the influence of other flow phenomena. Hopefully the results are in much better agreement with the reference solution than previous results. With some of the errors removed, other challenging aspects of the modelling approach can be identified and studied further.

Even tough previous studies have not concluded the sources of the discrepancies between results obtained from RANS and LES, strong indications that separation has a significant influence on the validity of the results has been obtained. The purpose of the present work is to increase the knowledge regarding the flow and modelling challenges in regions with separation and transient wake movement (i.e vortex shedding).

A well studied case which has been exposed to extensive research is the flow past slender cylinders. Cylinders with both cylindrical and square cross sections have been investigated with the consequence of a wide range of available results and knowledge. The flow is characterised by a number of flow phenomena, where many constitutes challenges in terms of modelling. It contains separation and reattachment, regions with recirculating flows, highly anisotropic turbulence and strong vortex shedding.

Slender and bluff bodies is a common geometric feature in engine bays. Hoses, pipes and ducts, such as exhaust manifolds, all provides conditions for vortex shedding. Many of the available references are conducted at Reynolds numbers comparable to those found for these components. With a maximum velocity magnitude in the region of $5 - 7\ m/s$ and length scales in the region of $50\ mm$, Reynolds numbers up to $2.5 \cdot 10^4$ can be expected. For geometries of circular cross section, this gives a sub-critical flow where the boundary layer is laminar in the region upstream of the separation point. This is however dependent on the turbulence level within the engine bay around and prior to these geometries. The turbulence level in an engine bay is expected to be rather low since the incoming free stream velocity from the environment is rather low. The relaminarizating properties of the radiator whose geometry is similar to that of flow straightener used in wind tunnels to reduce the turbulence level also reduces the turbulence level. The use of a sub-critical flow is therefore believed to be highly relevant for the application.

1.4 Limitations

A car is a complex system in which all sub-systems interact and affects both each other and the total performance of the car. The engine bay is no exception. The cooling system and the aero-thermal conditions in the engine bay affects several aspects of the cars performance. It can for example be noise generation by the fan and cooling air ducts, or the aerodynamic drag of the car. It is known that a considerable amount of drag is generated by conventional inlet and outlet configurations of cooling air. As high as $7 - 10$ % of the total drag has been reported by Khaled et al. [13] to be generated by the configuration of the cooling system. The focus of this study is strictly limited to the aero-thermal conditions and accuracy of modelling within the engine bay. How the conditions inside the engine bay affects the surroundings and other performance aspects is not included.

1.4.1 Ethical & ecological issues

The increased accuracy of the predicted thermal loads are not only advantageous when it comes to the performance of the developed cars. Increased accuracy is also advantageous when it comes to the ecological footprint. Uncertainties in technical development are always present to some degree. These uncertainties are often dealt with by adjusting the specifications of individual component. This could in turn results in an unnecessary consumption of material, a restriction to specially adapted materials, increased aerodynamic drag or unnecessary long duration of operation for the cooling fan, where all of which increases the environmental impact. By increasing the accuracy of the numerical methods, these uncertainties can be reduced and as a result enables cars which are better adapted for their range of operation.

The results could possible be used to develop cars with shorter life expectancy but that has a similar level of durability. This development would most likely increase the total environmental impact. In that case the use of the results becomes an ethical issue. This project will only cover the development of the numerical methods and not the way in which the results are used.

2 Theory

The available literature regarding the complete flow situation inside an engine bay is scarce, both for experimental and numerical work. Some work has been focused on specific aspects of the aero-thermal conditions, such as soaking or fan modelling. These studies are often limited to a specific region in the engine bay and/or conducted on simplified geometries. One example is the work of Gullberg [10] whose research included fan modelling in steady state solvers.

2.1 Flow past slender cylinders

The flow field past cylinders of different cross section is a common geometry seen in many engineering applications and have, because of this, been studied for many years. Early research have been focused on the global parameters of the flow such as coefficient of drag, fluctuating coefficient of lift, distribution of the pressure coefficient and Strouhal number at different Reynolds numbers. The coefficients of drag and lift is defined as $C_{d/l} = 2F/\rho U_\infty^2 A_c$, where F is either the drag or lift force on the cylinder and U_∞ the free stream velocity. The Strouhal number describes the shedding frequency, f_s, and is normalised with the free stream velocity, U_∞, and the diameter, D, and is defined as $St = f_s D/U_\infty$. The Reynolds number uses the diameter as characteristic length and is defined as $Re_d = U_\infty D/\nu$. During the last decades have knew technology, in the form of computers and laser based measuring techniques, enabled researchers to look closer into the characteristics of the wake in therms of the mean velocity field and turbulent quantities in different regions surrounding the cylinders. More extensive data regarding the size of the wake including parameters such as separation position & angle, recirculation region length (l_R), maximum wake with (l_w) and its location (x_w), some of which are illustrated in Figure 2.1, has been published both through numerical and experimental investigations.

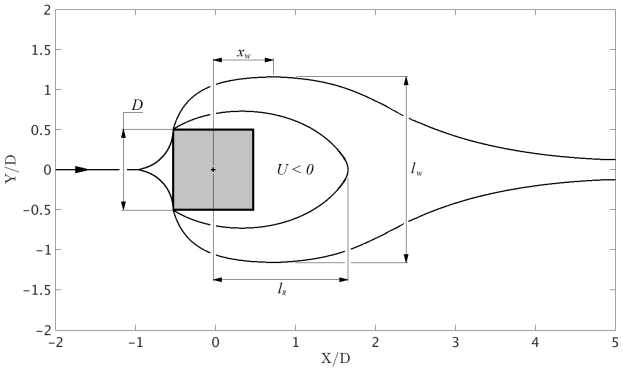

Figure 2.1: *Definition of the of characteristic lengths describing the wake.*

The vortex shedding process is characterised by a periodic movement of the wake behind bluff bodies. As the flow passes moves the wake from side to side and each time it does so a vortex is released down stream. The vortices originates from the sides of the body with an alternating side of origin for each vortex, which gives the vortices an alternating direction of rotation. As the vortices are transported down stream a von Kármán vortex street is created in its wake, illustrated in Figure 2.2.

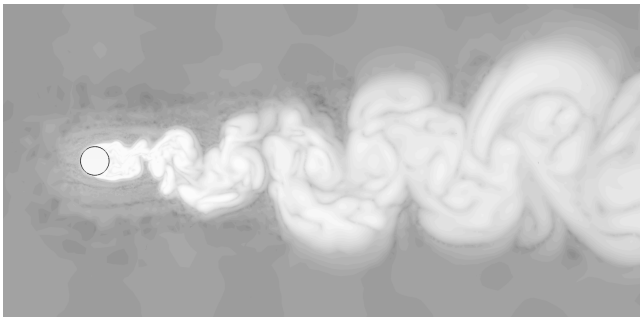

Figure 2.2: *Vorticity created by the vortex shedding process in the wake behind a cylinder with circular cross section.*

When investigating the flow quantities, they are typically decomposed into a time averaged, a coherent (periodically varying) and a incoherent (random) component. For the velocity, the decomposition can be written as

$$u_i = \overline{u_i} + \tilde{u}_i + u_i' \qquad \langle u_i \rangle = \overline{u_i} + \tilde{u}_i \tag{2.1}$$

where $\overline{u_i}$ is the constant time averaged value, $\overline{u_i}$ the periodic and u_i' the random velocity fluctuations.

The flow past cylinders of both circular and polygonal cross sections causes the flow to separate along the sides of the body. Since the flow in the boundary layer before the separation point can be both laminar (subcritical), transitional (critical) or fully turbulent (supercritical) can the separation behaviour and the flow be very different and difficult to model. In this study subcritical flows are investigated, meaning that the flow before the separation point is laminar. The transition to turbulent are induced by the separation

itself. As pointed out by Balzer & Fasel [1], the transition is due to separation created by the amplification of disturbances by the reverse flow velocity profiles, i.e the free shear layer between the free stream fluid and the fluid within the separation bubble. Independent of the turbulence level prior to separation, the disturbances will grow and induces roll-up of the shear layer into larger vortices or "rollers", which are convected down stream into the wake region where they are released down stream. It is this process which creates the vortex shedding process and due to the high level of anisotropy of the roll-up is it difficult to model.

The vortex shedding process is governed by different flow phenomena in different regions of the flow. The roll-up in the free shear layer at the separations is one of these regions. Further down stream the flow is governed by other flow phenomena. Lyn et al. [16] made a distinction between the regions down stream of the cylinder. As the vortices created in the free shear layers are transported downstream their size and behaviour changes. In the first four diameters, called the base region, the flow is characterised by strong mixing between the free stream fluid and the fluid within the base region. In this region the vortices grows and evolves into a fully developed von Kármán vortex street. In the fully developed vortex street, called the near wake, the vortices have a more stable size and behaviour.

The topology of the flow field in the near wake contains a number of interesting points. Perry & Steiner [21] showed the importance of the topology for the turbulence in the near wake. Along the vortex street occurs streamline saddle and centre points. The saddle points are identified as the region where two opposing flow streams meet and are redirected in the orthogonal directions. These saddle points creates high Reynolds shear stresses and production of turbulent kinetic energy. The streamline centres are regions completely enclosed by streamlines. The high production of turbulence in the saddle points are convected along the streamlines into the vortex centre, which results in a maximum of turbulent kinetic energy in the centres.

2.2 Turbulence modelling

The Navier-Stokes equations describes the movement and transport of momentum within the fluid.

$$\rho\frac{\partial u_i}{\partial t}+\rho\frac{\partial u_i u_j}{\partial x_j}=-\frac{\partial P}{\partial x_i}+\mu\frac{\partial^2 u_i}{\partial x_j\partial x_j} \tag{2.2}$$

$$\frac{\partial u_i}{\partial x_i}=0 \tag{2.3}$$

Time averaging as $\overline{u_i}=\frac{1}{2T}\int_{-T}^{T}u_i dt$ gives the Reynolds Averaged Navier-Stokes (RANS) equations.

$$\rho\frac{\partial \overline{u}_i\overline{u}_j}{\partial x_j}=-\frac{\partial \overline{P}}{\partial x_i}+\frac{\partial}{\partial x_j}\left(\mu\frac{\partial \overline{u}_i}{\partial x_j}-\rho\tau_{ij}\right) \tag{2.4}$$

$$\frac{\partial \overline{u}_i}{\partial x_i}=0 \tag{2.5}$$

If separation of scales is assumed, where the variations of the periodic field ($\tilde{u}_i$) are assumed to be much slower than the turbulent fluctuations (u_i'), the time gradient in equation (2.2) can be kept. The instantaneous time averaged velocity is defined as above according to $\langle u_i\rangle=\overline{u_i}+\tilde{u}_i$.

$$\rho\frac{\partial\langle u_i\rangle}{\partial t}+\rho\frac{\partial\langle u_i\rangle\langle u_j\rangle}{\partial x_j}=-\frac{\partial\langle P\rangle}{\partial x_i}+\frac{\partial}{\partial x_j}\left(\mu\frac{\partial\langle u_i\rangle}{\partial x_j}-\rho\tau_{ij}\right) \tag{2.6}$$

$$\frac{\partial\langle u_i\rangle}{\partial x_i}=0 \tag{2.7}$$

The new term, $\tau_{ij}=-\rho\overline{u_i'u_j'}$, in equation (2.4) and (2.6) are the Reynolds stresses which are modelled.

If equation (2.2) and (2.3) instead are averaged in space as $\hat{u}_i(x,t)=\frac{1}{\Delta x}\int_{x-0.5\Delta x}^{x+0.5\Delta x}u_i(\xi,t)d\xi$ the following equations are obtained

$$\rho\frac{\partial \hat{u}_i}{\partial t}+\rho\frac{\partial \hat{u}_i\hat{u}_j}{\partial x_j}=-\frac{\partial \hat{P}}{\partial x_i}+\frac{\partial}{\partial x_j}\left(\mu\frac{\partial \hat{u}_i}{\partial x_j}-\rho\hat{\tau}_{ij}\right) \tag{2.8}$$

$$\frac{\partial \hat{u}_i}{\partial x_i}=0 \tag{2.9}$$

With equation (2.8) and (2.9) can parts of the turbulence be resolved and computed with higher accuracy. The unknown sub-grid stress, $\hat{\tau}_{ij} = \widehat{u_i u_j} - \hat{u}_i \hat{u}_j$, which describes the unresolved turbulence appears and needs modelling similar as for the Reynolds stresses in the RANS approach.

2.2.1 Eddy viscosity models

Eddy viscosity models are the most common turbulence models used for engineering applications due to their low computational cost and stability. The convective influence from the turbulence on the transport of momentum, the Reynolds stresses, are modelled as an extra diffusion term through an eddy viscosity, μ_t. The models are based on Boussinesqs assumption who in 1877 found that the Reynolds stresses appeared to be linearly proportional to the strain rate tensor.

$$-\rho\overline{u_i' u_j'} = 2\mu_t S_{ij} - \frac{2}{3}\rho k \delta_{ij} \tag{2.10}$$

with $S_{ij} = \frac{1}{2}\left(\frac{\partial \overline{u}_i}{\partial x_j} + \frac{\partial \overline{u}_j}{\partial x_i}\right)$ and $\delta_{ij} = 1$ if $i = j$ and 0 if $i \neq j$. The second term in equation (2.10) is added to obtain the physically correct turbulent kinetic energy, k, as $\overline{u_i' u_i'} = 2k$. This second term is used to compute the Reynolds stresses but when implemented into CFD codes, such as Star CCM+, the second term is often excluded and said to be included in the pressure as $P_B = P + \frac{2}{3}\rho k \delta_{ij}$. The Reynolds stresses in equation (2.4) and (2.6) are therefore equal to $2\mu_t S_{ij}$ for the eddy viscosity models.

The eddy viscosity is assumed to have the same dimension as the dynamic viscosity, μ, which through dimensional analysis gives

$$\mu_t = C\rho\vartheta\ell \tag{2.11}$$

where ϑ is the turbulent velocity scale and ℓ the turbulent length scale. All eddy viscosity models uses Boussinesqs assumption to compute the Reynolds stresses but approximates the turbulent scales from different turbulent quantities obtained from additional transport equations or algebraic expressions.

A majority of the eddy viscosity models uses the modelled k-equation, which is given by

$$\rho\frac{\partial k}{\partial t} + \rho\frac{\partial k\langle u_i\rangle}{\partial x_i} = \frac{\partial}{\partial x_i}\left[\left(\mu + \frac{\mu_t}{\sigma_k}\right)\frac{\partial k}{\partial x_i}\right] + P^k - \rho\epsilon \tag{2.12}$$

$k-\omega$ SST

Menter [19] proposed a new alternative to the two common turbulence models $k-\epsilon$ and Wilcox $k-\omega$. Menter found that $k-\epsilon$ was much less sensitive toward assumed values of the model constants in the free stream, giving more accurate results then $k-\omega$. However, $k-\omega$ performes better in boundary layer flows with adverse pressure gradient. Menter proposed a model combining the two models. For $k-\epsilon$ are the turbulent viscosity and the velocity and length scales modelled as

$$\vartheta = k^{1/2} \qquad \ell = \frac{k^{3/2}}{\epsilon} \qquad \mu_t = \rho C_\mu \vartheta \ell = \rho C_\mu \frac{k^2}{\epsilon} \tag{2.13}$$

$k-\omega$ SST uses the same transport equations as $k-\epsilon$, i.e. the k-equation defined by equation (2.12) and the ϵ-equation, but with ϵ expressed as $\epsilon = \beta^* k\omega$. For incompressible flow the ϵ-equation then becomes

$$\rho\frac{\partial \omega}{\partial t} + \rho\frac{\partial \omega\langle u_i\rangle}{\partial x_i} = \frac{\partial}{\partial x_i}\left[\left(\mu + \frac{\mu_t}{\sigma_{\omega,1}}\right)\frac{\partial \omega}{\partial x_i}\right] + 2\gamma_2\rho S_{ij}\cdot S_{ij} - \beta_2\rho\omega^2 + 2\frac{\rho}{\sigma_{\omega,2}\omega}\frac{\partial k}{\partial x_i}\frac{\partial \omega}{\partial x_i} \tag{2.14}$$

The eddy viscosity are given by

$$\mu_t = \frac{a_1\rho k}{max(a_1\omega, SF_2)} \tag{2.15}$$

$$S = \sqrt{2S_{ij}S_{ij}} \qquad F_2 = tanh\left(max\left(\frac{2\sqrt{k}}{\beta^*\omega d}, \frac{500u}{d^2\omega}\right)^2\right)$$

The production turbulent kinetic energy and dissipation rate in equation (2.12) are given by

$$P^k = min\Big(10\beta^*\rho k\omega, 2\mu_t S_{ij}\cdot S_{ij}\Big) \qquad P^\epsilon = \beta^* k\omega \tag{2.16}$$

Table 2.1: *$k-\omega$ SST model constants.*

σ_k	$\sigma_{\omega,1}$	$\sigma_{\omega,2}$	γ_2	β_2	β^*	a_1	C_μ
1.0	2.0	1.17	0.44	0.083	0.09	0.31	0.09

The $k-\omega$ model is known to model the turbulent quantities in boundary layers correctly. $k-\omega$ SST is transformed into a $k-\omega$ model in boundary layer flows, which mean that it is possible to use the model in its original form all the way into the viscous sub-layer.

$k-\epsilon$ Realizable

Shih et al. [25] proposed a new $k-\epsilon$ model. The new model was based on the standard $k-\epsilon$ model with a modified transport equation for the dissipation rate, ϵ, and a new realizable eddy viscosity which would ensure physically correct non-negative normal Reynolds stresses. The model uses the modelled k-equation defined by equation (2.12). The ϵ-equation is defined as

$$\rho\frac{\partial\epsilon}{\partial t}+\rho\frac{\partial\epsilon\langle u_i\rangle}{\partial x_i} = \frac{\partial}{\partial x_i}\left[\left(\mu+\frac{\mu_t}{\sigma_\epsilon}\right)\frac{\partial\epsilon}{\partial x_i}\right]+C_{\epsilon,1}\rho S\epsilon-C_{\epsilon,2}\rho\left(\frac{\epsilon^2}{k+\sqrt{\nu\epsilon}}-\frac{k\epsilon_0}{(k+\sqrt{\nu\epsilon})max(k_0/\epsilon_0, C_t\sqrt{\nu/\epsilon_0})}\right) \tag{2.17}$$

with

$$C_{\epsilon,1} = max\left(0.43, \frac{\eta}{5+\eta}\right) \qquad \eta = \frac{\sqrt{2S_{ij}S_{ij}}k}{\epsilon}$$

The last term in equation (2.17), containing the ambient turbulence values ϵ_0 and k_0, was proposed by Spalart et al. [28] to counteract turbulence decay. The eddy viscosity is obtained as

$$\vartheta = k^{1/2} \qquad \ell = \frac{k^{3/2}}{\epsilon} \qquad \mu_t = \rho C_\mu\frac{k^2}{\epsilon} \tag{2.18}$$

with

$$C_\mu = \frac{1}{A_0 + A_s\sqrt{S_{ij}S_{ij}+\Omega_{ij}\Omega_{ij}}k/\epsilon} \qquad A_0 = 4$$

$$A_s = \sqrt{6}\cos\left(\frac{1}{3}\cos^{-1}\left(\sqrt{6}W\right)\right) \qquad W = S_{ij}S_{jk}S_{ki}/(S_{ij}S_{ij})^{3/2}$$

Table 2.2: *$k-\epsilon$ Realizable model constants.*

σ_k	σ_ϵ	$C_{\epsilon,2}$	A_0	C_{max}	C_{r1}	C_{r2}
1.0	1.2	1.9	4.0	1.25	0.04645	0.25

P^k and P^ϵ in equation (2.12) is defined as

$$P^k = min\left(C_{max}, \frac{1}{C_{r1}(|\eta|-\eta)+\sqrt{1-min(C_{r2},0.99)}}\right)\left(\mu_t S^2-\frac{2}{3}\rho k\frac{\partial\langle u_i\rangle}{\partial x_i}-\frac{2}{3}\mu_t\frac{\partial^2\langle u_i\rangle}{\partial x_i^2}\right) \tag{2.19}$$

$$P^\epsilon = \rho(\epsilon-\epsilon_0) \tag{2.20}$$

Unlike the $k-\omega$ models are the $k-\epsilon$ models unable to resolve the viscous sub-layer. To be able to do so the original model must be modified. Normally this is done by adjusting the model coefficients in the boundary layers to obtain physically more correct predictions. Rodi [23] proposed an alternative two-layer approach in

which the dissipation rate close to the wall is prescribed algebraically and then blended with the free stream values predicted by the ϵ-equation. ϵ are prescribed according to

$$\epsilon = \frac{k^{3/2}}{l_\epsilon} \tag{2.21}$$

The blending of the prescribed ϵ and the modelled one are provided by a wall-proximity indicator suggested by Jongen [12] as

$$\lambda = \frac{1}{2}\left(1 + tanh\left(\frac{Re_w - 60}{10/atanh(0.98)}\right)\right) \tag{2.22}$$

with

$$Re_w = \frac{\sqrt{k}d}{\nu}$$

The eddy viscosity is then defined as

$$\mu_t = \lambda\mu_{t,k-\epsilon} + (1-\lambda)\left(\frac{\mu_t}{\mu}\right)_{2layer} \tag{2.23}$$

$\mathbf{k-\epsilon\ \overline{v_2'^2}f}$

Similarly as for the $k-\epsilon$ model the transport equations for k and ϵ are solved for in the $k-\epsilon\ \overline{v_2'^2}f$ model. Beyond these two transport equations are two additional equations solved, one for the wall normal Reynolds stress $\overline{v_2'^2}$ and one for an elliptic damping function f. The reason for solving these extra equation is to more accurately capture the dampening of the wall normal turbulence than can be provided by the damping functions used for the two equation $k-\epsilon$ and $k-\omega$ models. The model is based on the work of Durbin [8], Lien et al. [15] and was further modified by Davidsson et al. [7]. The eddy viscosity is computed as

$$\mu_t = \rho \cdot min\left(C_\mu k max\left(k/\epsilon, C_t\sqrt{\nu/\epsilon}\right), C_{\mu_\vartheta 2}\overline{v_2'^2}max\left(k/\epsilon, C_t\sqrt{\nu/\epsilon}\right)\right) \tag{2.24}$$

The transport equations read

$$\rho\frac{\partial\epsilon}{\partial t} + \rho\frac{\partial\epsilon\langle u_i\rangle}{\partial x_i} = \frac{\partial}{\partial x_i}\left[\left(\mu + \frac{\mu_t}{\sigma_\epsilon}\right)\frac{\partial\epsilon}{\partial x_i}\right] + C_{\epsilon,1}\rho\frac{\epsilon}{k}\left(1 + A\sqrt{\frac{k}{\overline{v_2'^2}}}\right) - C_{\epsilon,2}\rho\left(\frac{\epsilon^2}{k} - \frac{\epsilon_0}{max(k_0/\epsilon_0, C_t\sqrt{\nu/\epsilon_0})}\right) \tag{2.25}$$

$$\rho\frac{\partial\overline{v_2'^2}}{\partial t} + \rho\frac{\partial\overline{v_2'^2}\langle u_i\rangle}{\partial x_i} = \frac{\partial}{\partial x_i}\left[\left(\mu + \frac{\mu_t}{\sigma_{\overline{v_2'^2}}}\right)\frac{\partial\overline{v_2'^2}}{\partial x_i}\right] + P^{\overline{v_2'^2}} - \frac{6\rho\overline{v_2'^2}\epsilon}{k} \tag{2.26}$$

$$L^2\frac{\partial^2 f}{\partial x_i^2} - f + P^f = 0 \tag{2.27}$$

with

$$P^{\overline{v_2'^2}} = \rho \cdot min\left(kf, -\frac{1}{max(\epsilon/k, C_t\sqrt{\nu/\epsilon})}\left((C_1-6)\overline{v_2'^2} - \frac{2k}{3}(C_1-1)\right) + C_2\left(\mu_t S^2 - (2/3)\rho k\nabla\mathbf{u} - (2/3)\mu_t(\nabla\mathbf{u})^2\right)\right)$$

$$L = C_L \cdot max\left(\frac{k^{3/2}}{\epsilon}, C_\eta\left(\frac{\nu^3}{\epsilon}\right)^{1/4}\right)$$

$$P^f = \frac{1}{max(\epsilon/k, C_t\sqrt{\nu/\epsilon})}(C_1-1)\left(\frac{2}{3} - \frac{\overline{v_2'^2}}{k}\right) + C_2\frac{C_{\mu\overline{v_2'^2}}\overline{v_2'^2}S^2}{\epsilon} + \frac{5\overline{v_2'^2}}{k\cdot max(\epsilon/k, C_t\sqrt{\nu/\epsilon})}$$

P^k in equation (2.12) is defined as

$$P^k = \mu_t S^2 - \frac{2}{3}\rho k \frac{\partial u_i}{\partial x_i} - \frac{2}{3}\mu_t \frac{\partial^2 u_i}{\partial x_i^2} \tag{2.28}$$

Table 2.3: *$k-\epsilon\ \overline{v_2'^2}f$ model constants.*

C_1	C_2	$C_{\epsilon 1}$	$C_{\epsilon 2}$	C_μ	$C_{\mu\overline{v_2'^2}}$	C_L	C_t	C_η	σ_k	σ_ϵ	$\sigma_{\overline{v_2'^2}}$	A
1.4	0.3	1.4	1.9	0.09	0.22	0.23	6	70	1	1.3	1	0.045

Unlike the original $k-\epsilon$, the $k-\epsilon\ \overline{v_2'^2}f$ model are able to compute the flow all the way into the viscous sub-layer, which means that no low Reynolds modification is needed in order to resolve the boundary layers.

Spalart-Allmaras

Spalart & Allmaras [29] proposed a one equation eddy viscosity model in which only one transport equation is solved for a kinematic eddy viscosity parameter, $\tilde{\nu}$. The eddy viscosity is computed as

$$\mu_t = \rho\tilde{\nu} f_{\nu 1} \tag{2.29}$$

The transport equation for $\tilde{\nu}$ reads

$$\rho\frac{\partial\tilde{\nu}}{\partial t} + \rho\frac{\partial\tilde{\nu}\langle u_i\rangle}{\partial x_i} = \rho C_{b,1}(1-f_{t2})\tilde{S}\tilde{\nu} + \frac{1}{\sigma_\nu}\left[\frac{\partial}{\partial x_i}\left((\mu+\rho\tilde{\nu})\frac{\partial\tilde{\nu}}{\partial x_i}\right) + C_{b,2}\rho\frac{\partial^2\tilde{\nu}}{\partial x_i^2}\right] - \rho\left(C_{\omega 1}f_\omega - \frac{C_{b1}}{\kappa^2}f_{t2}\right)\left(\frac{\tilde{\nu}}{d}\right)^2 \tag{2.30}$$

with

$$f_{t2} = 1.1\cdot e^{-2\chi^2} \qquad \chi = \frac{\tilde{\nu}}{\nu}$$

$$\tilde{S} = \sqrt{2\mathbf{\Omega_{ij}}\mathbf{\Omega_{ij}}} + \frac{\tilde{\nu}}{\kappa^2 d^2}f_{\nu 2} \qquad C_{\omega 1} = \frac{C_{b1}}{\kappa^2} + \frac{1+C_{b2}}{\sigma_{\tilde{\nu}}} \qquad f_{\nu 2} = 1 - \frac{\chi}{1+\chi f_{\nu 1}}$$

$$f_\omega = g\left(\frac{1+C_{\omega 3}^6}{g^6+C_{\omega 3}^6}\right)^{1/6} \qquad g = min\left(\frac{\tilde{\nu}}{\tilde{S}\kappa^2 d^2}, 10\right) \qquad f_{\nu 1} = \frac{\chi^3}{\chi^3 + C_{\nu 1}^3}$$

Table 2.4: *Spalart-Allmaras model constants.*

C_{b1}	C_{b2}	$C_{\omega 2}$	$C_{\omega 3}$	κ	σ_ν	$C_{\nu 1}$
0.1355	0.622	0.3	2.0	0.41	2/3	7.1

The original proposed model included an additional trip term, $\rho f_{t1}\Delta\langle\mathbf{u}_i\rangle^2$, which is used to initiate boundary layer transition. This term is not included in the implementation in Star CCM+.

The Spalart-Allmaras model, just like $k-\omega$, is a low Reynolds model in its original form, which means that it can be used all the way into the viscous sub-layer.

2.2.2 Reynolds Stress Model

Unlike the eddy viscosity models, the Reynolds stress model (RSM) solves the Reynolds stresses directly by solving their transport equations. Even though the Reynolds stresses are obtained from their respective transport equations, modelling is needed to determine a number of the terms in their equations. The transport equation for the Reynolds stresses reads

$$\rho\frac{\partial\tau_{ij}}{\partial t} + \rho\frac{\partial\tau_{ij}\langle u_k\rangle}{\partial x_k} = \frac{\partial}{\partial x_k}D_{ijk}^\tau + P_{ij}^\tau + \underline{\phi} + \underline{\epsilon} \tag{2.31}$$

with

$$P_{ij}^{\tau} = -\rho\left(\tau_{ik}\frac{\partial\langle u_j\rangle}{\partial x_k} + \tau_{jk}\frac{\partial\langle u_i\rangle}{\partial x_k}\right)$$

The turbulent diffusion term, D^{τ}, the turbulent dissipation, $\underline{\epsilon}$, and the pressure-strain term, $\underline{\phi}$, needs modelling as follows

$$D_{ijk}^{\tau} = \left(\mu + \frac{\mu_t}{\sigma_k}\right)\frac{\partial\tau_{ij}}{\partial x_k} \tag{2.32}$$

ϵ is obtained from the modelled ϵ-equation from the standard $k-\epsilon$ model.

$$\rho\frac{\partial\epsilon}{\partial t}+\rho\frac{\partial\epsilon\langle u_i\rangle}{\partial x_i} = \frac{\partial}{\partial x_j}\left[\left(\mu+\frac{\mu_t}{\sigma_\epsilon}\right)\frac{\epsilon}{\partial x_j}\right]+\frac{\epsilon}{k}\left(C_{\epsilon 1}\frac{1}{2}P_{kk}-C_{\epsilon 2}\rho\epsilon\right)+A_1\nu(\tau_{lm}N_{lm})\frac{k}{\epsilon}(1-\alpha^3)\left(\frac{\partial}{\partial x_n}((S_{op}n_p)^{1/3}n_n)\right)^2 \tag{2.33}$$

The pressure-strain term is obtained using the elliptic blending model proposed by Lardeau & Manceau [14].

$$\underline{\phi}-\underline{\epsilon} = (1-\alpha^3)(\underline{\phi}^{\omega}-\underline{\epsilon}^{\omega})+\alpha^3(\underline{\phi}^{h}-\underline{\epsilon}^{h}) \tag{2.34}$$

with

$$\alpha - L^2\nabla^2\alpha = 1$$

$$\underline{\phi}_{ij}^{h} = -(C_1\rho\epsilon+C_{1s}P_{kk}))A_{ij}+(C_3-C_{3s}\sqrt{A_{lm}A_{lm}})\rho kS_{ij}+C_4\rho k(S_{in}A_{nj}+A_{io}S_{oj}-\frac{2}{3}A_{pq}S_{pq}))+C_5\rho k(\Omega_{ir}A_{rj}+A_{is}\Omega_{sj})$$

$$A_{ij} = \frac{\tau_{ij}}{k}-\frac{2}{3}\delta_{ij}$$

$$\underline{\phi}_{ij}^{\omega} = -5\rho\frac{\epsilon}{k}(\tau_{ik}N_{kj}+\tau_{il}N_{lj}-\frac{1}{2}\tau_{mn}N_{mn}(N_{ij}+\delta_{ij})) \qquad N_{ij} = n_in_j \qquad n_i = \frac{\partial\alpha/\partial x_i}{\sqrt{\partial\alpha/\partial x_j\cdot\partial\alpha/\partial x_j}}$$

$$\underline{\epsilon}^{h} = \frac{2}{3}\epsilon\delta_{ij} \qquad \underline{\epsilon}^{\omega} = \tau_{ij}\frac{\epsilon}{k} \qquad L = C_1 max\left(\frac{k^{3/2}}{\epsilon}, C_\eta\frac{\nu^{3/4}}{\epsilon^{1/4}}\right)$$

In equation (2.33) is the eddy viscosity needed. It is redefined as

$$\mu_t = \rho C_\mu k\cdot max\left(\frac{k}{\epsilon}, C_t\sqrt{\frac{\nu}{\epsilon}}\right) \tag{2.35}$$

Table 2.5: *RSM model constants.*

σ_k	σ_ϵ	C_M	C_s	$C_{\epsilon 1}$	$C_{\epsilon 2}$	C_μ	A_1	C_1
1.00	1.15	2.00	0.21	1.44	1.83	0.07	0.115	1.70
C_{1s}	C_3	C_{3s}	C_4	C_5	C_l	C_t	C_ν	
0.90	0.80	0.65	0.625	0.20	0.133	6.00	80.0	

The RSM with elliptic blending function is a low Reynolds model, which means that it can be used all the way into the viscous sub-layer.

2.2.3 Smagorinsky model

The subgrid stresses in equation (2.8) needs modelling. The first developed model for these stresses where the Smagorinsky model developed by Smagorinsky [26]. The modelling of the subgrid stresses is, similar to the eddy viscosity models, based on Boussinesqs assumption as

$$\hat{\tau}_{ij} = 2\mu_t S_{ij} - \frac{2}{3}\rho k\delta_{ij} \tag{2.36}$$

The Smagorinsky model approximates μ_t as

$$\mu_t = \rho\Delta^2 S \tag{2.37}$$

with

$$\Delta = f_\nu min(\kappa d, C_s V^{1/3}) \qquad f_\nu = 1 - e^{-y^+/A}$$

Table 2.6: *Smagorinsky model constants.*

C_s	A
0.1	25

2.2.4 Detached Eddy Simulations

Even though the RANS and scale resolving appraches uses different averageing techniques there are no difference between equation (2.6) and (2.8). Menter & Kuntz [20] proposed a mix between the approaches which is called Detached Eddy Simulations (DES). It uses unsteady RANS in the boundary layers and LES in the free stream. The turbulent quantities are described using k and ω, which are solved for using equation (2.12) and (2.14) from the $k-\omega$ SST model. The transition to LES is provided by modifying the specific dissipation rate, ω, as

$$\tilde{\omega} = \omega\phi \tag{2.38}$$

with

$$\phi = max\left(\frac{l_t}{C_{DES}\Delta}F, 1\right) \qquad F = 1 - tanh\left(\left(\frac{2\sqrt{k}}{\beta^*\omega d}, \frac{500\nu}{d^2\omega}\right)^2\right)$$

$$C_{DES} = C_{DES,k-\omega}F_1 + C_{DES,k-\epsilon}(1-F_1) \qquad F_1 = tanh\left(\left(min\left(max\left(\frac{\sqrt{k}}{0.09\omega d}, \frac{500\nu}{d^2\omega}\right), \frac{2k}{d^2 CD_{k\omega}}\right)\right)^4\right)$$

$$CD_{k\omega} = max\left(\frac{1}{\omega}\nabla k \cdot \nabla\omega, 10^-20\right) \qquad l_t = \frac{\sqrt{k}}{\beta^*\omega}$$

Table 2.7: *Detached Eddy Simulation model constants.*

$C_{DES,k-\omega}$	$C_{DES,k-\epsilon}$
0.78	0.61

* *Other model constants are defined as in the $k-\omega$ SST model above.*

2.3 Resolution of Scale Resolving Methods

For scale resolving methods the mesh is of great importance. There are a number of strategies to evaluate the mesh ability to resolve turbulent length scales. Among these are evaluation of the resolved energy, two point correlation and different ratios of the modelled sub-grid scale quantities to resolved or mean quantities. Quantities such as: shear stress, viscosity, dissipation and kinetic energy can be used. Previous investigations by Davidsson [6][5] has shown that among these, the two point correlation is the most accurate.
The two point correlation is a tool used for evaluating how closely the fluctuations of a quantity in two different points are related. A high value indicates that if the quantity increases in one of the points, it is likely to also increase in the other. A value close to zero indicates that the fluctuations in the two are completely uncorrelated and changes independently of each other. A large negative value indicates that the fluctuations in the two point are correlated but that an increase in one point is likely to result in a decrease in the other.
The two point correlation is defined as

$$B_{ij}(x, \hat{x}) = \overline{v_i'(x)v_j'(x+\hat{x})}. \tag{2.39}$$

It is often normalised by $v_{i,rms}(x)v_{j,rms}(x+\hat{x})$ where $v_{i,rms}(x) = \sqrt{v_i'^2}$.

$$B_{ij}^{norm}(x,\hat{x}) = \frac{\overline{v_i'(x)v_j'(x+\hat{x})}}{v_{i,rms}(x)v_{j,rms}(x+\hat{x})} \tag{2.40}$$

Note that in a direction in which the turbulence is homogeneous $\frac{\partial v_{i,rms}}{\partial \hat{x}}$, which makes $v_{i,rms}(x) = v_{i,rms}(x+\hat{x})$. Equation (2.40) then becomes a function of only the distance between the two points, $\hat{x}$.
By investigating the correlation of velocity fluctuations in two points it can be determined if the two points are enclosed by the same eddies at the same time. As one of the point is moved further from the other the correlation will decrease. At a certain distance the correlation will approach zero, indicating that the distance between the points is larger than the resolved turbulence. The number of points within this distance gives a number on the resolution of the turbulent length scales. Davidsson [5] suggested that for a coarse LES a resolution of at least 8 cells should be used.
The two point correlation do not just give a measure of how well the turbulent length scales are resolved, it also gives a measure of the size of the large scales. The integral length scale, i.e. the size of the large turbulent scales, can be determined as

$$\ell(x) = \int_0^\infty \frac{B_{ij}(x,\hat{x})}{v_{i,rms}(x)v_{j,rms}(x+\hat{x})} d\hat{x}. \tag{2.41}$$

3 Method

The simplified geometry chosen as validation case is based on the work of Xu et al. [30], who investigated the flow around slender cylinders of varying cross sections at a number of Reynolds numbers ranging from $Re_d = 1 \cdot 10^4$ to $1 \cdot 10^5$ in an open loop wind tunnel. The experimental study included investigation and comparison of coefficient of drag, fluctuating lift coefficient, Strouhal number, critical Reynolds number at which the boundary layer transitions to a turbulent behaviour, separation point and topology of the wake in therms of recirculation region length (l_R), wake width (l_w) and position of the maximum width stream wise location (x_w).

The different cross sections consisted of a variety of polygonal shapes, categorised into different groups depending on their orientation and shape. The different orientations consisted of geometries with a face or a corner normal to the incoming flow, denoted as "F" (face) or "C" (corner) geometries respectively. The shape of the cross sections was defined by the number of sides, i.e. a geometry with four sides is named "4". Combining the two parameters, a geometry with four sides with a face oriented with its normal parallel to the incoming flow is named "4F". The same geometry rotated 45° so that a corner is pointing towards the incoming flow the geometry is named "4C". The investigated geometries included shapes of 2-8, 12 and 16 sides of both "F" and "C" orientation.

This validation case is relevant for a number of reasons. It contains the flow phenomena that are difficult to model, described in Section 2.1. With a Reynolds number of $Re_d = 1 \cdot 10^4$ and a diameter $D = 25\,mm$ the free stream velocity for air at a standard atmosphere ($101325\,Pa$ and $288.15\,K$) becomes $5.87\,m/s$, both a length scale and velocity comparable to those found in an engine bay. This ensures that the flow phenomena behaves in a similar way as in an engine bay. The large variation of polygonal shapes also gives a large platform for evaluating different turbulence models and numerical setups ability to predict the separation in great detail. The different geometries has different separation behaviour, which has been divided into three categories by Xu et al. [30]: $\{i\}$ The flow separates at the corner farthest from the centre line (defined as T_0) and do not reattach $\{ii\}$ The flow separates at the corner farthest from the centre line (T_0), even though there are one corner up-stream from the separation point, and do not reattach $\{iii\}$ The flow separates at the corner up stream from the corner that is farthest from the centre line (defined as T_1) and reattach and separates again at the corner farthest from the centre line (T_0) $\{iv\}$ The flow separates at the corner up stream from the corner that is farthest from the centre line (T_1) and do not reattach. By testing the numerical setups for geometries from the different separation groups, their ability to predict separation can be evaluated. The tested geometries are presented in Figure 3.1.

The present study investigated the cross sections illustrated in Figure 3.1: 2F, 4F$\{i\}$, 7F $\{ii\}$, 7C $\{iv\}$, 8C $\{iii\}$ and 16C. 2F was also investigated due to being a common geometric feature in engine bays.

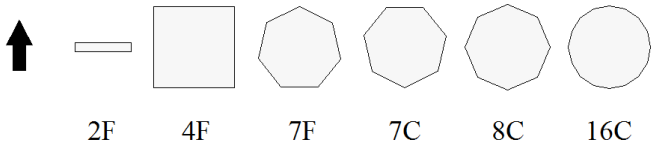

Figure 3.1: *Tested geometries with an arrow indicating the free stream flow direction.*

Several parameters was measured and compared to the experimental data, including coefficient of drag, recirculation region length, wake width and Strouhal number. The Strouhal number was determined from a fast Fourier transform performed on the velocity magnitude in a point located $2.5D$ down stream from the cylinder centre.

3.0.1 Computational domain & Mesh for RANS computations

The computational domain was kept as similar as possible to the wind tunnel experiment with a cross section of $0.5 \times 0.5\,m$. The wind tunnel section is extended $10D$ $(0.25\,m)$ up stream and $20D$ down stream. The length of the test cylinder was $16.8D$ $(0.42\,m)$, giving an aspect ratio of 16.8 and a blockage of $\alpha \approx 5\,\%$, due to end plates that reduced the influence of both the boundary layers along the walls and 3D effects. A Cartesian coordinate system is defined with origin positioned in the centre of the cylinder at the mid span in the span wise direction. The x-axis is pointing in the down stream direction and the z-axis is in the span wise direction.

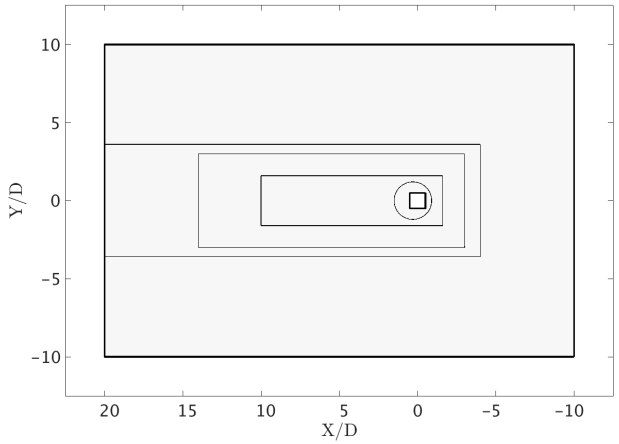

Figure 3.2: *Location and sizes of local mesh refinements.*

The mesh was created using polyhedral cells to reduce the effect of false diffusion. A total of three box refinements and a cylinder refinement was added around the cylinder and in its wake according to Figure 3.2. The cell sizes was set according to Table 3.1. The cell size in the local refinements is presented in relation to the largest cell size in the free stream, referred to as base size.

Table 3.1: Mesh refinement.

Refinement box	Stream-wise length $[x/D]$	Sideways width $[y/D]$	cell size [%]
Base size	-	-	100
Coarse	$[-20D\ +4D]$	$\pm 3.6D$	75
Medium	$[-14D\ +3D]$	$\pm 3D$	50
Fine	$[-10D\ +1.6D]$	$\pm 2.4D$	25
Cylinder	Diameter $= 2.4D$, centred at $x = -0.3D$		15

Along the walls of both the wind tunnel and the cylinder, prism layer is added. The thickness of the first layer is adjusted to give y^+-values below 1. The growth of the prism layer follows a geometric progression adjusted both to give a smooth transition in size from the last prism layer to the bulk cells and to get a total thickness similar to the boundary layer thickness.

In order to determine the required cell size a mesh study was performed, in which the number of prism layers and base size was investigated. The base size was varied as $\Delta x = 20$ $(\Delta x/D = 0.8)$, 15 $(\Delta x/D = 0.6)$, 10 $(\Delta x/D = 0.4)$ and $8\,mm$ $(\Delta x/D = 0.32)$. From the result in Figure 3.3, it can be seen that only

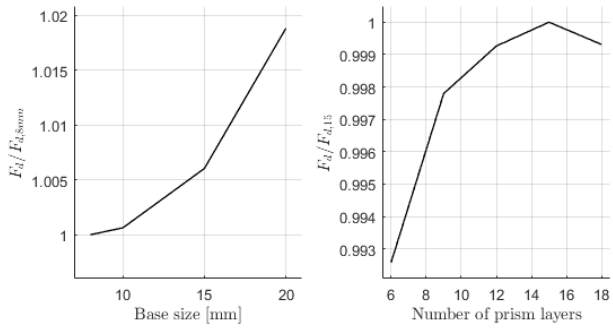

Figure 3.3: *Results for the mesh study obtained from the geometry 4F with $k-\omega$ SST. The results for the drag on the cylinder are normalised by the results from the finest mesh resolutions.*

marginal differences in the result can be seen. However, the drag force on the cylinder seems to have reached a converged state at $10\,mm$, which was chosen for future computations. The number of prism layers were varied as 6, 9, 12, 15 and 18 for which the results can be seen in Figure 3.3. These results was obtained with a base size of $10\,mm$. An even smaller variation of the result was observed and 15 was chosen as the number of prism layers. Since the aim of the present study is to investigate the numerical setup rather than the mesh, a larger number of prism layers was chosen to reduce the mesh dependency and make sure that the resolution is fine enough even with geometric variations. This could be permitted due to the limited increase in cell count. The refinement boxes was also both extended to the outlet and made wider with negligible effect on the result.

3.0.2 Computational domain & Mesh for scale resolving methods

To be able to resolve the turbulent scales a mesh that is significantly finer than that of RANS simulations is needed. This is especially true for LES computations near walls which puts stringent size limitations in both the wall normal and parallel directions. To limit the computational power needed to perform the computations the domain was reduced and only the geometry 4F and a circular cylinder were considered. The walls and the height of the domain were removed and reduced. Instead of having a cylinder shorter than the height of the test section combined with end plates to retain a 2-dimensional mean field the cylinder was extended to span the entire height. The walls was changed to symmetry planes and the boundaries in the span wise direction was changed to periodic boundary conditions. The height was reduced to $0.25\,m$ ($10D$) compared to the original height of $0.5\,m$, giving a new aspect ratio of 10. Similar studies have used similar dimensions but with a smaller aspect ratio. Sohankar et al. [27] used a domain with a length of $24.2D$, a width of $15.7D$ and a height of varying from $4D$ to $7D$. Elkhoury [9] used a domain that was $20.5D$ long, $14D$ wide and $4D$ high for URANS simulations. The reason for using a higher aspect ratio is that Sohankar et al. [27] found that as the aspect ratio was increased from 4 to 7, the rms lift and drag were reduced with 3 and 15%, indicating a dependence on the aspect ratio. An aspect ratio of 10 was used in order to reduce these effects.

The mesh strategy used for the scale resolving methods was quite different from that used for the RANS simulations. To be able to resolve the turbulence correctly a specific number of cell is needed to resolve the large turbulent eddies. The size of the large turbulent length scales varies within the domain, variations which is difficult to adapt a mesh to by using local mesh refinements built up by simple geometric features. Drastic changes in cell size between the refinements and poor adaptation to the flow field can result in large variations in resolution. Instead of using local mesh, the cell sizes was related to the large turbulent length scales. Even though the URANS simulations do not resolve the turbulent length scales they can be approximated from the modelled quantities that are used to describe the turbulence. For $k-\epsilon$, k describes the turbulent kinetic energy and ϵ the destruction of turbulent kinetic energy. The destruction takes place at the smallest turbulent scales if the turbulent kinetic energy is assumed to be conserved throughout the cascade process. Even if ϵ is used to describe a phenomena taking place at the small scales it can be related to the large scales trough the conservation of energy which gives equilibrium of production of turbulent kinetic energy at the large scales and destruction at the smallest scale. The large scales are approximated as $\ell = k^{3/2}/\epsilon$ and with $\epsilon = \beta^* k\omega$ ($\beta^* = 0.09$)

$$\ell = \frac{\sqrt{k}}{\beta^*\omega} \tag{3.1}$$

The basic principle of the meshing approach is to evaluate equation (3.1) for the results obtained from a transient $k-\omega$ SST simulation to approximate the size of the large scale turbulence as a continuously varying field in the entire domain. The size of the turbulence can then be divided by a constant n_c to get the cell size, Δx, required to resolve a large scale eddy by n_c cells in the entire domain.

$$\Delta x = \frac{1}{n_c} \cdot \frac{\sqrt{k}}{\beta^*\omega}$$

To include the surface cell size was the equation adjusted according to

$$\Delta x = max\left(\frac{1}{n_c} \cdot \frac{\sqrt{k}}{\beta^*\omega}, \Delta x_s\right) \tag{3.2}$$

where Δx_s is the surface cells size. This implementation of a surface cell size is possible due to the fact that the predicted large turbulent length scales approaches zero at the surfaces of the cylinder. By implementing the adjustment user control of the surface resolution is added.

Equation (3.2) was evaluated and used as a field function refinement for a polygonal mesher in STAR-CCM+ to obtain a mesh adapted to the flow field. k and ω was taken as the time averages $\overline{k}$ and $\overline{\omega}$. 15 and 30 prism layer was added on the surface of the cylinder in order to resolve the boundary layer down to $y+ < 1$ for the DES and LES meshes respectively.

3.0.3 Numerical setup

The flow was computed using the commercial software STAR-CCM+ version 12.06.010 and with a number of modelling approaches, including RANS, DES and LES. For the RANS approach a number of turbulence models and both a steady state solver and a unsteady solver (URANS) was used. It was expected that the steady state solver would not give accurate results for such a transient flow. However, since steady state solver are used quite frequently it is of great interest to investigate how much and in what way it is incorrect. Both the steady state and transient solutions was computed as incompressible flows with a coupled pressure-velocity solver. The transient computations utilised an implicit solver with constant time steps.

The implemented turbulence models include $k-\epsilon$ Realizable and $k-\omega$ SST, Reynolds Stress Model (RSM) with elliptic blending, the four equation $k-\epsilon$ $\overline{v_2'^2}f$ and the one equation Spalart Allmaras. The $k-\epsilon$ models are known for their inability to model the shear stress in boundary layers with adverse pressure gradient and therefore has difficulty predicting separation. However, the two modified versions investigated in this study are better adapted to other flow phenomena present in this kind of flow, such as predicting the turbulent production in the stagnation region in front of the cylinder, which makes them interesting to investigate. The $k-\omega$ SST and the RSM both have desirable features for the current flow, such as better prediction of boundary layers in separating flows. RSM have additional advantages compared to the eddy viscosity models due to the fact that it can handle anisotropic turbulence and curvature effects. The Spalart Allmaras has the advantage of being computationally efficient due to being a one equation model. It was developed and are used for airfoils and has proved reliable for separating flows.

For the RANS solutions the 3^{rd}-order MUSCL up-wind scheme was used for the momentum equations and the 2^{nd}-order upwind scheme for the turbulent quantities. The transient implicit solver used a time step of $1.125 \cdot 10^{-4}\,s$ ($tU_\infty/D = 0.0264$) and 15 iterations per time step. All turbulence models was initialised from a solution obtained with $k-\omega$ SST that had been running for ($3\,s \cdot 5.866\,ms^{-1}/0.75\,m > 20$ flow through times). Sampling of mean field quantities started after yet another flow through time and continued for 38 flow through times. This was a large value, considerably higher than those used in similar studies, and could have been reduced. The convergence of the mean quantities was controlled by the mean drag and lift on the cylinder, which indicated a fully developed behaviour.

For the LES the Smagorinsky sub-grid stress model was used with $C_s = 0.1$. A bounded central differencing scheme was used for the momentum equations and the 2^{nd}-order upwind scheme for the turbulent quantities. The time step was reduced to $5.33 \cdot 10^{-5}\,s$ ($tU_\infty/D = 0.0125$) and the initialisation was done similar to the URANS computations with the difference that the sampling of mean field quantities started after $1\,s$ (7.8 flow through times) and continued for $2\,s$ (15.6 flow through times). The DES used a numerical setup similar to what was used for the LES solution with $k-\omega$ SST for the URANS part.

3.0.4 Boundary conditions

The wind tunnel walls and the surface of the cylinder was set to no-slip walls and at the outlet the pressure was specified and all other quantities extrapolated from the up stream cells. At the inlet a turbulent intensity of $\hat{\epsilon} = 0.05\%$, similar to what was measured in the experiment, and a viscosity ratio of 10 was specified. Prior to the computations the influence of the boundary layer thickness on the solution was investigated. It was found that the drag increased by 2.4 % with a fully developed boundary layer compared to a constant velocity profile at the inlet. The velocity profile with a boundary layer was obtained by extending the inlet $2\,m$ upstream. In order to replicate the experimental setup as much as possible it was assumed that a fully developed boundary layer was present. The temperature was set to $288.15\,K$ giving a viscosity of $\mu = 1.7965 \cdot 10^{-5}\,Pa \cdot s$. To obtain a Reynolds number of $Re_d = 1 \cdot 10^4$, a free stream velocity of $U_\infty = 5.87\,m/s$ was specified.

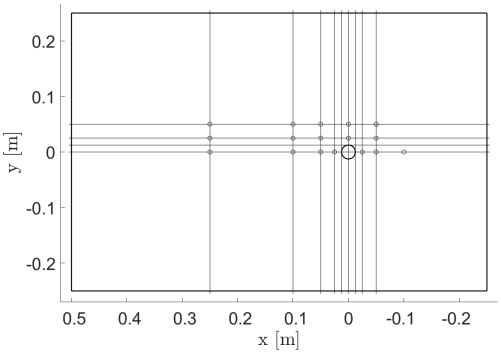

Figure 3.4: *The instantaneous velocities was sampled along several lines, in both x-, y- and the homogeneous z-direction. The thin solid lines illustrates the sampling lines in the x- and y-direction and the circles illustrates the sampling lines in the z-direction.*

3.0.5 Evaluation of resolution for scale resolving mesh

In order to evaluate the mesh of the scale resolving methods two point correlations was used. A number of sampling lines, illustrated in Figure 3.4, was added prior to the simulations along which the instantaneous velocities for u, v and w was extracted at each time step and cell centre of the cells intersecting the line. Two point correlations was then computed between all of the point along the sampling lines and the number of neighbouring nodes with a non-zero correlation was counted using a MATLAB script. The non-zero correlation was defined as a normalised correlation value above 0.3 and the count was taken from the direction with the least amount of cells above the threshold value. By using a $n_c = 8$ and limiting the cell size above $\Delta x_s/D = 0.032$ the resolution of the large turbulent length scales could not be kept above 8 cells per eddy and the obtained y^+ value was above one, which meant that thickness of the surface cells had to be reduced. Instead was n_c increased to 10 and the thickness reduced to $\delta/D = 4 \cdot 10^{-4}$. To keep the maximum aspect ratio of the cells below 10 along the walls was the surface cell size limited to $\Delta x_s/D = 0.008$. The minimum cell size along the surfaces for the square cross section gave a resolution of 125 cells per side, a significantly larger number than 25 cells used by Sohankar et al. [27]. Even with the new settings the resolution was still not good enough close to the cylinder surface with a number of locations at which the resolution was below 8.

Figure 3.5a and 3.5b illustrates a typical distribution of the obtained resolution. It appears that the lowest resolution is found for the two point correlations in the homogeneous z-direction. The reason for this might be that the mean field are two dimensional in the xy-plane, which means that the mean velocity gradients are only non-zero in these two directions. Turbulence is generated by the amplification of disturbances due to gradients in the mean field. This would indicate that the production of turbulence takes place in the xy-plane. Newly created turbulence is highly anisotropic and has large turbulent length scales. The large length scales are broken down in the cascade process, which turns large anisotrpoic scales into many small isotropic scales. This means that the turbulent length scales found in the z-direction are not generated by the gradients in the mean field but are a result of larger scales being turned into smaller ones with different orientations. They are therefore smaller than those found in the xy-plane. The scale resolving methods wants to resolve the largest scales of the turbulence and a result, a finer resolution is needed in the homogeneous direction.

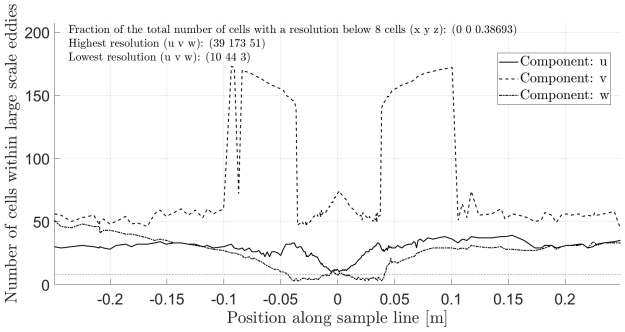

(a) *The resolution varies in the domain. In the wake are the scales small and puts the most stringent requirement on the resolution. The current distribution of resolution is taken at a line in the y-direction at $x = -10D$ and $z = 0$.*

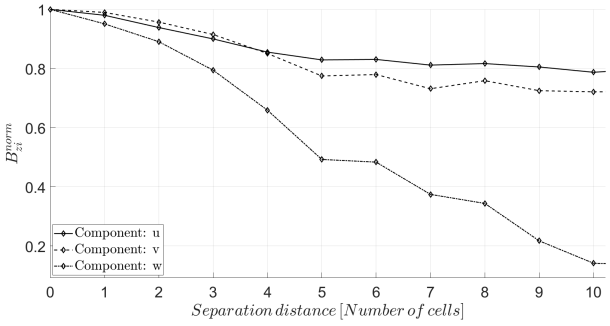

(b) *Resolution along sampling line oriented in the z-direction at $x = -4D$ and $y = 1D$.*

Figure 3.5

4 Results

The main purpose of using the experimental study performed by Xu et al. [30] is to investigate different turbulence models ability to predict separation and reattachment for a set of cylinders with different polygonal cross sections. The polygonal shapes all exhibit different behaviour of separation and reattachment, including complex flows with multiple separation and reattachment points, giving a wide variety of different flows which must be handled correctly by the turbulence model.

The results, including separation point, coefficient of drag (C_d), recirculation region length (l_R), wake width (l_w) and Strouhal number (St), are obtained at a Reynolds number of $Re_d = 1 \cdot 10^4$ and compared to the experimental results obtained by Xu et al. [30]. The separation point was identified as the point at which the streamwise velocity becomes negative. The separation point is often defined as the point in which the skin friction coefficient, defined as $C_f = 2\tau_w/\rho U_\infty^2 = 2\mu \frac{\partial u}{\partial y}_{y=0}/\rho U_\infty^2$, changes sign. In extension this gives the same definition as the velocity changing direction. The global characteristics of the wake were defined according to Section 2.1 and all length parameters are normalised by D and velocities by U_∞.

4.0.1 Predictions of separation & reattachment

Table 4.1 summarises the separation points obtained with the different turbulence models. The results are generally in good agreement with the experimental results. For the steady RANS only two cases were incorrectly predicted, both with the turbulence model $k-\epsilon$ Realizable and for the geometries 7C and 16C. In both cases the separation behaviour is underestimated with a delayed separation. For 16C the separation is postponed entirely and separation does not occur until T_0, compared to T_1 indicated by the experiments. For 7C is the separation at T_1 captured but the separation bubble collapses before reaching T_0, causing the flow to reattach. The separation behaviour becomes similar to that of 8C, which has a similar geometry but with a slightly blunter angle at the corners.

The predicted separation is worse for the unsteady RANS. It is still the same geometries that constitutes a challenge but in addition to $k-\epsilon$ Realizable, several of the other turbulence model are incapable of predicting the separation correctly. RMS, Spalart-Allmaras and $k-\epsilon$ Realizable predicts a separation and reattachment before T_0 for the geometry 7C. All turbulence models predict separation at T_0 instead of T_1 for the geometry 16C.

Common for both RANS and URANS is that if the separation is incorrectly predicted, it is under predicted. By the present author it is believed that this might be due to incorrectly modelled turbulence in the free stream and along the surface of the cylinder. From Balzer & Fasel [1] it is known that the turbulence level in the free stream and in the region close to a separation bubble can decrease the size of the bubble. Partly due to increased mixing in the boundary layer ahead if it, which prevents the boundary layer from separating in the first place by constantly transporting momentum into it, and partly due to entrainment of free stream fluid into the separation bubble itself. The entrianment is a transient phenomenon of the interface between the free stream fluid and the fluid contained inside the separation bubble. The interface is constantly moving due to large eddies passing by and occasionally large eddies can burst into the bubble causing it to collapse if it is small enough or otherwise drastically reduce its size. RANS does not resolve the turbulence and can therefore not capture this transient phenomena. The eddy viscosity RANS models investigated in this study models the convective transport of quantities due to turbulence as an extra diffusion term, in the form of an extra viscosity, μ_t. For $k-\epsilon$ Realizable, $k-\epsilon$ $\overline{v_2^2}f$ and $k-\omega$ SST μ_t are directly proportional to the turbulent kinetic energy k, according to equation (4.1). For Spalart-Allmaras μ_t is proportional to the kinematic eddy viscosity in a similar way. This means that an increased turbulent kinetic energy gives an increased viscosity and as a result an increased diffusion of streamwise momentum into the separation bubble. A higher streamwise momentum means that the low pressure zone in the recirculation region in the near wake will have smaller influence on the movement of the fluid. Instead of being slowed down and sucked into the recirculation region the fluid will have enough momentum to sustain a positive streamwise velocity, which thereby reduces the recirculation region length.

$$\mu_t = \rho C_\mu \frac{k^2}{\epsilon} \qquad \mu_t = k\frac{\rho a_1}{max(a_1\omega, SF_2)} \qquad \mu_t = \rho\tilde{\nu}f_{v1} \tag{4.1}$$

Table 4.1: *The predicted separation point compared to the experimental results. T_0 is defined as the corner farthest from the centre line and T_1 as the neighbouring corner up-stream from T_0. The entries highlighted in red indicates incorrect prediction of separation point for one or several turbulence models. For further details see explanation below.*

Geometry	RANS	URANS	Xu et al. [30]
2F	T_0	T_0	T_0
4F	T_0	T_0	T_0
7F	T_0	T_0	T_0
7C	T_1[1]	T_1[2]	T_1 (without reattachment)
8C	T_1	T_1	T_1 (with reattachment and separation again at T_0)
16C	T_1[3]	T_1[4]	T_1 (without reattachment)

[1] $k-\epsilon$ Realizable predicts separation at T_1 with reattachment and separation again at T_0.
[2] $k-\epsilon$ Realizable, RSM and Spalart-Allmaras predicts separation at T_1 with reattachment and separation at T_0.
[3] $k-\epsilon$ Realizable predicts separation at T_0.
[4] All turbulence models predict separation at T_0.

4.0.2 Wake characteristics

Table 4.2 and 4.3 summarises the results from the polygonal cylinder validation case for the steady and unsteady RANS respectively. The results obtained from the steady RANS are extremely different from the experimental results for all of the investigated parameters. The largest error obtained from the three parameters are those for the recirculation region length, which deviates by several hundred percent. The error for the width of the wake is also quite large with an error of around 50 % for many of the cases. Common for both the length of the recirculation region and the width of the wake is that the characteristic lengths of the wake is highly exaggerated. The coefficient of drag on the other hand is consistently underestimated by around 20 % depending on the geometry. This general trend appears to be consistent for all geometries with an exception for the prediction of the drag coefficient for geometry 8C which gives relatively acceptable results.

Among the turbulence models the results are also consistent, both in terms of the magnitude of the error for each model and the differences between them. The most obvious difference can be seen for Spalart-Allmaras which performs significantly better than the rest of the models for all of the investigated parameters. Even if Spalart-Allmaras have been used extensively and been proven to give reasonable results in aerospace applications, with similar flow conditions as in the present study, tests by Menter [18] have shown that $k-\omega$ SST have a similar and even better performance. It is therefore surprising that such a big difference can be observed. On the other side of the spectrum is RSM, which predicts the longest wake for all geometries. RSM is the most advanced of the investigated RANS models and computes the Reynolds stresses directly by solving six separate transport equations in contrast to the other four which models them through a linear relation between an eddy viscosity and the strain rate tensor. RSM can therefore, in contrast to the others, predict both the effects of anisotropic turbulence and curved streamlines better than the others. Since both of the effects are especially pronounced in the current flow significant differences can be expected, even though better results for RSM would have been expected. For $k-\omega$ SST, $k-\epsilon$ Realizable and $k-\epsilon$ $\overline{v_2'^2}f$ only comparatively small difference can be seen. $k-\epsilon$ $\overline{v_2'^2}f$ predicts slightly longer recirculation regions, but which of the other to performs the best appears to be rather random.

The results for the unsteady RANS is in much better agreement with the experimental results. However, relatively large differences are still present. Instead of over predicting the length of the recirculation region, it is under predicted by around 25 %. A similar reduction can be seen for the width of the wake. The general trends in the steady RANS can be seen also for the unsteady RANS. The errors for the length of the recirculation have the largest magnitude followed by the width of the wake. The coefficients of drag are predicted rather well for geometries with a small number of faces but increases compared to the experiments for the 8C and 16C geometries.

The differences between the models seen for the steady RANS changes somewhat for the unsteady solutions. Many of them can still be seen, but they are drastically decreased. Spalart-Allmaras which produced significantly better for the steady RANS now predicts results that are much closer to the other models, even though it still predicts shorter recircualtion regions in many of the cases. RSM still predicts relatively long and wide wakes, which in this case means better agreement with the experiments. Among the $k-\epsilon$ and $k-\omega$ models the accuracy for the different geometries are rather random. For the steady RANS was $k-\epsilon$ $\overline{v_2'^2}f$ predicting slightly longer recirculation regions. For the unsteady solutions this tendency has disappeared.

Table 4.2: Results for polygonal geometries using steady RANS at $Re_d = 1 \cdot 10^4$.

Geometry: 2F	$C_d/C_{d,exp} - 1$ [%]	$l_R/l_{R,exp} - 1$ [%]	$l_w/l_{w,exp} - 1$ [%]
$k-\omega$ SST	-28.87	224.50	54.12
$k-\epsilon$ Realizable	-30.27	207.97	51.59
RSM elliptic blending	-30.60	271.81	63.08
$k-\epsilon$ $\overline{v_2'^2}f$	-29.17	234.90	51.86
Spalart Allmaras	-15.56	24.43	4.78
Experiments by Xu et al. [30]	$C_{d,exp} = 2.250$	$l_{R,exp} = 3.15D$	$l_{w,exp} = 1.80D$

Geometry: 4F	$C_d/C_{d,exp} - 1$ [%]	$l_R/l_{R,exp} - 1$ [%]	$l_w/l_{w,exp} - 1$ [%]
$k-\omega$ SST	-21.69	382.92	56.17
$k-\epsilon$ Realizable	-25.83	401.52	58.70
RSM elliptic blending	-25.00	496.47	71.28
$k-\epsilon$ $\overline{v_2'^2}f$	-23.76	416.02	54.11
Spalart Allmaras	-15.51	138.71	20.41
Experiments by Xu et al. [30]	$C_{d,exp} = 2.100$	$l_{R,exp} = 1.85D$	$l_{w,exp} = 1.70D$

Geometry: 7F	$C_d/C_{d,exp} - 1$ [%]	$l_R/l_{R,exp} - 1$ [%]	$l_w/l_{w,exp} - 1$ [%]
$k-\omega$ SST	-35.79	250.38	42.00
$k-\epsilon$ Realizable	-40.27	277.37	49.43
RSM elliptic blending	-38.50	326.24	56.66
$k-\epsilon$ $\overline{v_2'^2}f$	-36.75	273.81	43.10
Spalart Allmaras	-26.67	81.28	15.42
Experiments by Xu et al. [30]	$C_{d,exp} = 1.663$	$l_{R,exp} = 1.80D$	$l_{w,exp} = 1.30D$

Geometry: 7C	$C_d/C_{d,exp} - 1$ [%]	$l_R/l_{R,exp} - 1$ [%]	$l_w/l_{w,exp} - 1$ [%]
$k-\omega$ SST	-30.24	404.21	46.32
$k-\epsilon$ Realizable	-43.53	344.20	25.12
RSM elliptic blending	-35.10	389.95	58.10
$k-\epsilon$ $\overline{v_2'^2}f$	-31.79	348.24	50.08
Spalart Allmaras	-29.78	105.35	13.36
Experiments by Xu et al. [30]	$C_{d,exp} = 1.228$	$l_{R,exp} = 1.40D$	$l_{w,exp} = 1.20D$

Geometry: 8C	$C_d/C_{d,exp} - 1$ [%]	$l_R/l_{R,exp} - 1$ [%]	$l_w/l_{w,exp} - 1$ [%]
$k-\omega$ SST	-7.78	290.57	47.34
$k-\epsilon$ Realizable	-8.68	266.79	36.42
RSM elliptic blending	-11.00	347.11	48.84
$k-\epsilon$ $\overline{v_2'^2}f$	-8.51	292.32	40.05
Spalart Allmaras	6.16	112.42	25.72
Experiments by Xu et al. [30]	$C_{d,exp} = 0.950$	$l_{R,exp} = 1.35D$	$l_{w,exp} = 1.10D$

Geometry: 16C	$C_d/C_{d,exp} - 1$ [%]	$l_R/l_{R,exp} - 1$ [%]	$l_w/l_{w,exp} - 1$ [%]
$k-\omega$ SST	-17.63	231.29	41.45
$k-\epsilon$ Realizable	-34.24	182.78	18.90
RSM elliptic blending	-21.31	297.56	52.27
$k-\epsilon$ $\overline{v_2'^2}f$	-20.36	243.27	39.22
Spalart Allmaras	-10.89	83.00	15.94
Experiments by Xu et al. [30]	$C_{d,exp} = 1.050$	$l_{R,exp} = 1.50D$	$l_{w,exp} = 1.10D$

Table 4.3: Results for polygonal geometries using unsteady RANS at $Re_d = 1 \cdot 10^4$.

Geometry: 2F	$C_d/C_{d,exp} - 1$ [%]	$l_R/l_{R,exp} - 1$ [%]	$l_w/l_{w,exp} - 1$ [%]	$St/St_{exp} - 1$ [%]
$k-\omega$ SST	11.27	-37.59	-16.42	16.73
$k-\epsilon$ Realizable	5.80	-41.78	-17.37	13.75
RSM elliptic blending	18.70	-30.40	-21.59	15.24
$k-\epsilon\ \overline{v_2'^2}f$	12.62	-38.48	-17.59	15.24
Spalart Allmaras	11.48	-35.26	-16.39	13.25
Experiments by Xu et al. [30]	$C_{d,exp} = 2.250$	$l_{R,exp} = 3.15D$	$l_{w,exp} = 1.80D$	$St_{exp} = 0.143$

Geometry: 4F	$C_d/C_{d,exp} - 1$ [%]	$l_R/l_{R,exp} - 1$ [%]	$l_w/l_{w,exp} - 1$ [%]	$St/St_{exp} - 1$ [%]
$k-\omega$ SST	19.06	-39.23	-10.13	6.54
$k-\epsilon$ Realizable	5.15	-24.88	-6.39	13.00
RSM elliptic blending	10.14	-27.34	-6.13	10.31
$k-\epsilon\ \overline{v_2'^2}f$	11.69	-52.13	-10.74	13.54
Spalart Allmaras	16.86	-39.00	-11.32	6.01
Experiments by Xu et al. [30]	$C_{d,exp} = 2.100$	$l_{R,exp} = 1.85D$	$l_{w,exp} = 1.70D$	$St_{exp} = 0.132$

Geometry: 7F	$C_d/C_{d,exp} - 1$ [%]	$l_R/l_{R,exp} - 1$ [%]	$l_w/l_{w,exp} - 1$ [%]	$St/St_{exp} - 1$ [%]
$k-\omega$ SST	9.52	-34.79	-5.78	17.31
$k-\epsilon$ Realizable	-1.50	-40.87	-7.81	35.19
RSM elliptic blending	3.44	-27.21	-4.03	32.44
$k-\epsilon\ \overline{v_2'^2}f$	7.36	-35.79	-6.73	25.56
Spalart Allmaras	13.89	-35.96	-5.33	21.90
Experiments by Xu et al. [30]	$C_{d,exp} = 1.663$	$l_{R,exp} = 1.80D$	$l_{w,exp} = 1.30D$	$St_{exp} = 0.155$

Geometry: 7C	$C_d/C_{d,exp} - 1$ [%]	$l_R/l_{R,exp} - 1$ [%]	$l_w/l_{w,exp} - 1$ [%]	$St/St_{exp} - 1$ [%]
$k-\omega$ SST	-15.57	34.28	8.14	-47.27
$k-\epsilon$ Realizable	-3.13	-31.13	-6.25	-33.52
RSM elliptic blending	-11.84	-1.96	-2.00	-36.19
$k-\epsilon\ \overline{v_2'^2}f$	-16.14	8.76	0.31	-40.78
Spalart Allmaras	-6.89	-21.28	-5,83	-38.29
Experiments by Xu et al. [30]	$C_{d,exp} = 1.228$	$l_{R,exp} = 1.40D$	$l_{w,exp} = 1.20D$	$St_{exp} = 0.169$

Geometry: 8C	$C_d/C_{d,exp} - 1$ [%]	$l_R/l_{R,exp} - 1$ [%]	$l_w/l_{w,exp} - 1$ [%]	$St/St_{exp} - 1$ [%]
$k-\omega$ SST	37.45	-19.38	0.72	4.91
$k-\epsilon$ Realizable	52.14	-24.79	1.59	22.39
RSM elliptic blending	56.27	-15.27	1.77	18.75
$k-\epsilon\ \overline{v_2'^2}f$	59.88	-25.07	2.10	9.28
Spalart Allmaras	79.23	-25.81	1.13	8.18
Experiments by Xu et al. [30]	$C_{d,exp} = 0.950$	$l_{R,exp} = 1.35D$	$l_{w,exp} = 1.10D$	$St_{exp} = 0.195$

Geometry: 16C	$C_d/C_{d,exp} - 1$ [%]	$l_R/l_{R,exp} - 1$ [%]	$l_w/l_{w,exp} - 1$ [%]	$St/St_{exp} - 1$ [%]
$k-\omega$ SST	28.56	-27.16	-0.99	22.09
$k-\epsilon$ Realizable	-13.05	-14.88	-3.14	-24.36
RSM elliptic blending	20.25	-24.16	-1.83	35.48
$k-\epsilon\ \overline{v_2'^2}f$	21.97	-28.90	-2.62	24.01
Spalart Allmaras	30.67	-28.09	-1.48	17.49
Experiments by Xu et al. [30]	$C_{d,exp} = 1.050$	$l_{R,exp} = 1.50D$	$l_{w,exp} = 1.10D$	$St_{exp} = 0.185$

4.0.3 Vortex shedding process

The largest discrepancies in the results are those for the recirculation region length between the steady and unsteady solutions. As discussed above is it known that the transport of streamwise momentum into the wake due to turbulence has a large impact on the topology in regions with separated flows. In this case, however, is it believed that the extreme differences can not be the result of incorrectly modelled turbulence directly. The results from the steady and unsteady solvers both have similarities and differences. Upstream and closely downstream from the separation points the flow are rather steady, making the results from the steady RANS both more accurate and also more similar to those from the unsteady solver. The turbulence in these regions will therefore be equal for the two solvers, making the contribution to the transfer of momentum due to turbulence similar for the two cases. The difference in recirculation region length must therefore be the result of other sources affected by the resolved vortex shedding.

In order to understand the flow and the vortex shedding process is it important to understand the forces effecting the flow. For the proceeding analysis the geometry 4F will be investigated in further detail using $k-\omega$ SST. Just as for all the face oriented geometries the geometry 4F has a face normal oriented parallel to the incoming flow, which creates a high pressure stagnation region in front of the cylinder. The geometry is characterised by a number of separation points, all visible in Figure 4.1. The first two is created at the leading corners where the fluid has been pushed sideways by the high pressure zone, creating recirculation regions on the sides of the cylinder. As stated above, the flow in the regions in front of the cylinder centre is rather similar for both the steady and unsteady solvers. The unsteady vortex shedding process does however affect the flow upstream to some extent by moving the stagnation point slightly from side to side as the wake moves.

The large discrepancies are created downstream in the wake of the cylinder. The flow in this region is dominated by a low pressure zone created in the region behind the cylinder. This low pressure zone directs free stream fluid into the near wake and creates the major recirculation region. The recirculation regions, or vortices, are created and sustained by the interaction of the momentum brought into the wake by the free stream fluid and the low pressure zone near the centre of the vortex. The low pressure zone constantly redirects the momentum into a circular motion which in turn helps sustain the low pressure. The steady RANS predicts two stationary symmetric vortices. The unsteady RANS resolves the vortex shedding process and therefore is only one vortex present in the wake region closest to the cylinder at any given time. The created vortices has both an alternating direction of rotation and location of creation. The vortices are created at the corners in the back of the cylinder, where reattached flow from the side vortices separates once again and creates small recirculation regions. This behaviour is fundamentally different from how the vortices are created in the actual flow and is a result of the modelling approach. As stated in Section 2 the vortices is created by amplification of disturbances and roll-up in the free shear layers in the separated regions on the side of the cylinder. The RANS models are unable to resolve these small rollers.

The created vortices sticks to the back side of the cylinder and gradually increase in size as more fluid is accumulated in the vortex. It is during this part of the process the vortex grows and it is terminated when the vortex is finally saturated and is released downstream. It then travels backwards and slightly towards the opposite side of the cylinder from where it was first created.

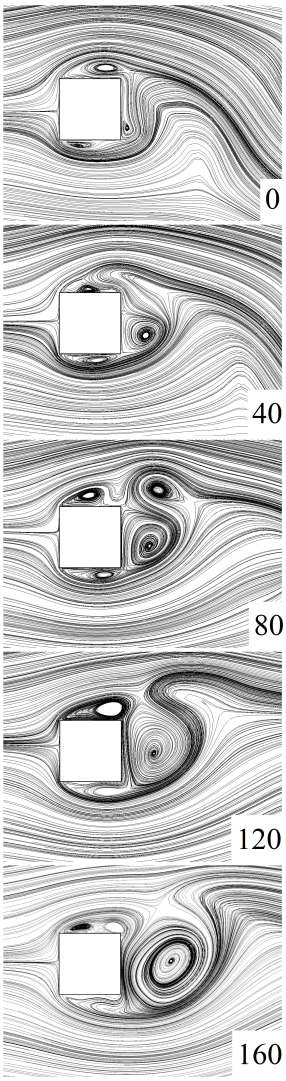

Figure 4.1: *Development of the flow fields topology at the time step* 0*,* 40*,* 80*,* 120 *and* 160*, at which the velocity magnitude (Figure 4.2), static pressure (Figure 4.3) and radial velocity (Figure 4.4) have been investigated. The* 0^{th} *time step is taken as a step in the early stage of the build-up. Up until the* 80^{th} *time step the vortex keeps growing but remains stuck to the cylinder surface. After the* 80^{th} *is the vortex released from the surface and starts moving downstream during which it starts to dissolve. One time step is* $\frac{\Delta t U_\infty}{D} = 0.026$*. Incoming flow from the left.*

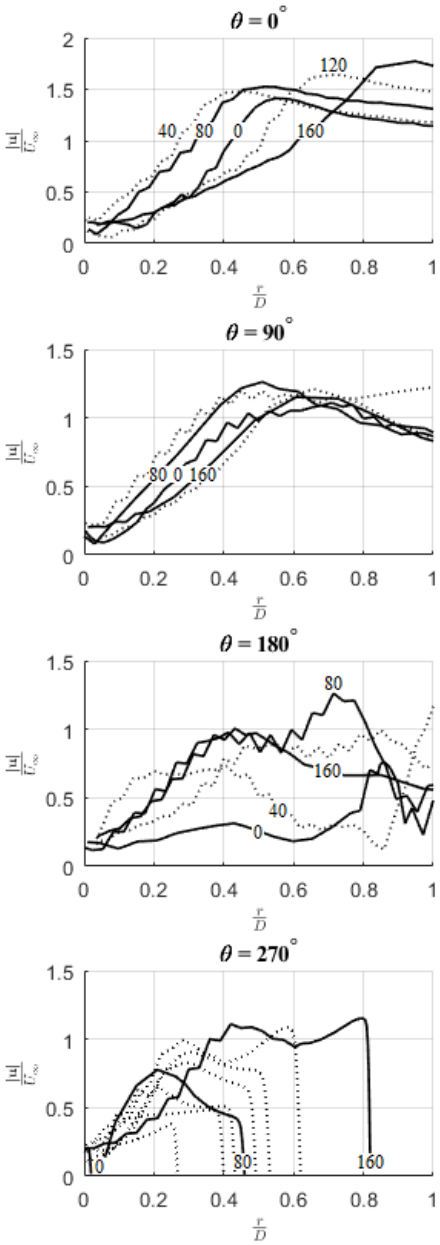

Figure 4.2: *Development of the velocity magnitude. The velocity magnitude is normalised with* U_∞ *and the radial position with* D*. The solid lines illustrates the distribution at time step* 0*,* 80 *and* 160*. The dashed lines illustrates the distribution at time step* 40 *and* 120*. At angle* $\theta = 270°$ *is more dashed lines added, which are separated by* 20 *time steps. One time step is* $\frac{\Delta t U_\infty}{D} = 0.026$.

Further downstream is the trajectory of the vortex changed and a movement parallel to the free stream is obtained. During the build-up, fluid is accumulated in the recirculation region on the opposite side of the cylinder from where the vortex is created, as shown in Figure 4.1 at time step 80 and 120. As the vortex is realised downstream the size of this region is reduced, as seen at time step 160, and the fluid is pulled into the back of the cylinder by the low pressure. This movement triggers the creation of a new separation and a new vortex. The new vortex undergoes the same process mirrored about the centre line as compared to the presiding vortex.

The resolved vortex shedding process is far more complex than the flow predicted by the steady RANS and it is obvious that it adds streamwise momentum to the fluid in the near wake, reducing the recirculation region length of the mean field. However, it is not obvious in what form the momentum is transferred into the wake. It is not crucial to understand how the transfer of momentum is different for the steady and unsteady simulations. That a steady solver are not able to predict an unsteady flow phenomena are expected. However, it is important to understand the transfer to be able to clarify what possible requirements it puts on the turbulence modelling and the unsteady numerical setup in general.

In order to investigate the variation of quantities, such as velocity, pressure and the terms in the momentum equation, at both different locations along the vortex and over time is a number of sampling lines added. A local cylindrical coordinate system that moves together with the vortex is added in the streamline centre of the vortex. The local z-axis is oriented parallel to the global negative z-axis and the angular position, θ, is defined as zero in the direction of the negative y-axis of the global coordinate system with its positive direction in the clock wise direction. The location of the centre for each time step is visually identified by computing the instantaneous streamlines and are updated at each time step. Four sampling lines are added in the coordinate system, all originating in the origin of the cylindrical coordinate system and are parallel with the r-axis at $\theta = 0°$, $90°$, $180°$ and $270°$. The duration of the sampling period is half a shedding cycle and covers the time from the creation of one vortex, the realise of the vortex from the cylinder surface and the initial part of its dissolution and transport downstream. The obtained data comes, as already mentioned, from the geometry 4F using unsteady $k-\omega$ SST. This analysis gives a very rough set of data, unsuitable for direct comparison with both other studies and different numerical setups, due to the vulnerability to variations in the investigated shedding cycle and the position of the local coordinate system. However, it can provide a more detailed view of different phases in the vortex shedding process than time averaged data. With a better knowledge of the local events in the shedding cycle more accurate and relevant time averaged data, more suitable for comparison, can be obtained later on.

The distributions of velocity magnitude, static pressure and radial velocity along the sampling lines are presented in Figure 4.2, 4.3 and 4.4, respectively. As it turns out the velocity magnitude varies extensively at both different locations around the vortex and over time. The free stream fluid enters the base region at $\theta = 0°$ for which the magnitude is highest. As the fluid moves around the vortex it is gradually reduced. When comparing the velocity at different time steps it can be seen that the magnitude increases. Both the magnitude at a specific radial distance from the vortex centre and the size of the vortex increases with time. The increase in size is clearly illustrated by the sampling line at $\theta = 270°$, which is directed upstream toward the back of the cylinder. The magnitude increases with increased distance to the vortex centre and when the wall is approached the velocity is abruptly reduced.

The location of the sudden drop in velocity gives a sense of the size and the development of the vortex. The increase in velocity magnitude is visible for all sampling lines. However, at around the 80^{th} time step the velocity appears to start to decrease for the sampling lines at $\theta = 0°$ and $90°$. This results in a movement of the location of the maximum velocity magnitude from $\theta = 0$ to $70°$. In Figure 4.1 it appears that free stream fluid starts to enter the region between the vortex and the cylinder at the 80^{th} time step, indicating that the velocity maximum follows the location where free stream fluid is brought into the base region.

The pressure distribution is illustrated in Figure 4.3. Compared to the velocity distribution the pressure is more evenly distributed along th four lines. Instead the largest variations is seen over time. Initially, at the 0^{th} time step, the pressure is rather high. As momentum is accumulated to the vortex and the velocity increases the pressure can be seen to decrease. As discussed before are the velocity and the pressure are related and from an increase in velocity are a decrease in pressure expected. Similarly when the velocity decreases an increase in pressure is expected. The velocity magnitude could be seen to start to decrease as the vortex is released from the cylinder at around the 80^{th} time step. However, it is not until the 160^{th} time step that the pressure can be observed to reach a minimum and start increase.

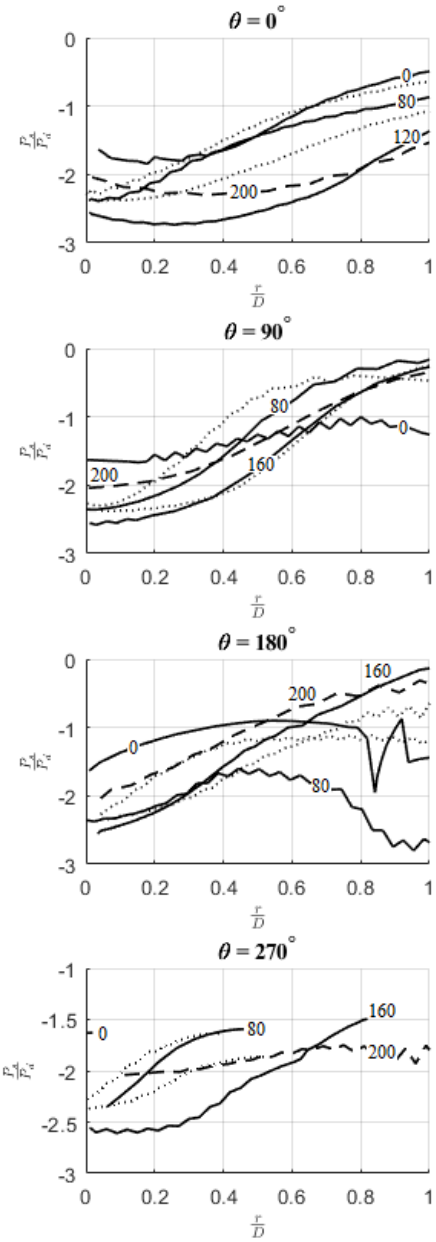

Figure 4.3: *Development of the static pressure. The pressure is normalised with the dynamic pressure* $P_d = \frac{1}{2}\rho U_\infty^2$ *and the radial position with* D*. The solid lines illustrates the distribution at time step* 0, 80 *and* 160*. The dashed lines illustrates the distribution at time step* 200*. One time step is* $\frac{\Delta t U_\infty}{D} = 0.026$.

4.0.4 Momentum transport

In order to investigate the changed flow condition and the phenomenons effecting the recirculaion region length the transfer of momentum into the wake will be investigated further. This is most efficiently done by investigating the different terms in the transport equation for the momentum, which in its time averaged state for incompressible flows reads

$$\rho\frac{\partial\langle u_i\rangle}{\partial t} = -\rho\frac{\partial\langle u_i\rangle\langle u_j\rangle}{\partial x_j} - \frac{\partial\langle P\rangle}{\partial x_i} + \frac{\partial}{\partial x_j}\left(\mu\frac{\partial\langle u_i\rangle}{\partial x_j} - \rho\langle u_i' u_j'\rangle\right) \quad (4.2)$$

$$\mathbb{R}ate\ of\ change = -\mathbb{C}onvection + \mathbb{P}ressure\ term + ...$$

$$... + (\mathbb{V}iscous\ diffusion + \mathbb{T}urbulent\ diffusion)$$

At first it was believed that the momentum is added to the wake mainly through the convection term, which describes the transfer of momentum due to the movement of a fluid. The convection term can describe the additional transfer of momentum created by free stream fluid entering the wake region as the wake oscillates from side to side due to the vortex shedding. The term would therefore be of great importance in this case and might explain the difference between the solvers. Even though this is true, is it not as simple as a direct relation between the averaged streamwise velocity and the convection term. As stated above there is a close relation between the convection term and the pressure term in which the pressure gradient redirects the movement into a circular motion. It is quite intuitive that a circular fluid motion would create centrifugal forces that has to be counteracted by a centripetal force, which in this case is created trough the pressure term. The streamwise momentum added by the free stream fluid entering the wake region will therefore to a large extent be counteracted by a pressure gradient. Since the momentum is not destroyed by the pressure term, merely redirected, the speed of the fluid should remain fairly unchanged ignoring the influence of diffusion. The streamwise velocity is reduced and transformed, first into a sideways and then into an upstream movement. At the upstream edge of the vortex the pressure term then help to recover the streamwise velocity.

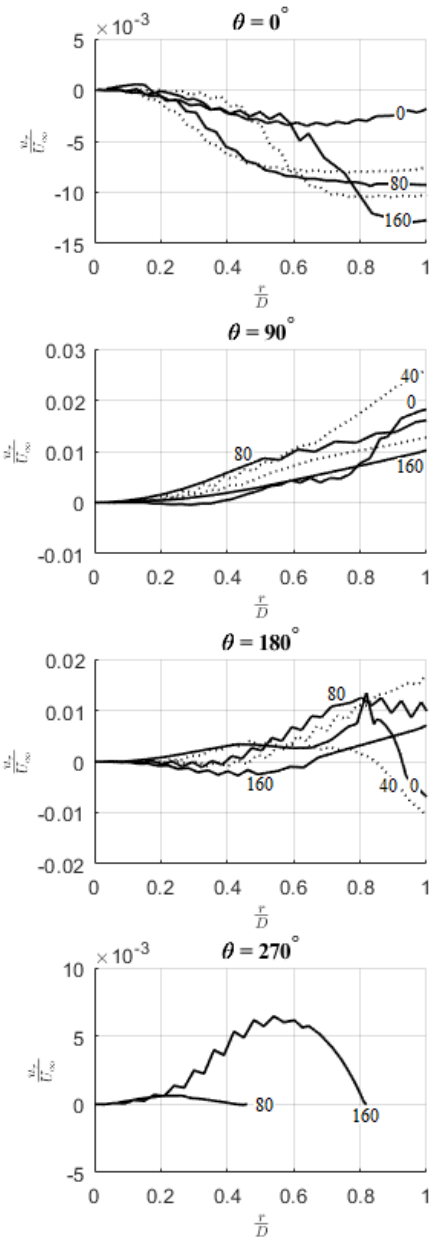

Figure 4.4: *Development of the radial velocity. The radial velocity is normalised with* U_∞ *and the radial position with* D*. The solid lines illustrates the distribution at time step* 0, 80 *and* 160*. The dashed lines illustrates the distribution at time step* 40 *and* 120*. One time step is* $\frac{\Delta t U_\infty}{D} = 0.026$*.*

As already mentioned the transport of momentum, and because of that, the acceleration of the fluid elements is dominated by the convection and pressure terms. Both the convection and pressure terms is in turn determined by the gradients of the velocity and pressure, respectively. The convection term can, with help of the continuity equation, be simplified as follows

$$-\mathbf{C} = -\rho \frac{\partial \langle u_i \rangle \langle u_j \rangle}{\partial x_j} = -\rho \langle u_j \rangle \frac{\partial \langle u_i \rangle}{\partial x_j} \tag{4.3}$$

Due to the curved streamlines created by the circular motion inside the vortex the gradients of the velocities will be both large and sensitive to topological changes of the vortex, especially in regions of the vortex where the streamlines deviate from a circular topology and creates a protrusion with sharper curvature. The pressure gradient along the sampling lines, as illustrated by Figure 4.3, varies with the distance to the vortex centre. Just as for the convection this gives a sensitive behaviour toward topological changes. Situations in which the vortex centre and the low pressure minimum do not coincide or when protruding streamlines with an elliptic shape are present this should give rise to a retardation of the velocity as the streamlines moves out from the centre and the low pressure region and acceleration when moving towards it. Figure 4.1 illustrates the development of the flow topology during the creation and shedding of a vortex. It can be seen that the topology deviates quite extensively from a circular one during the initial creation of the vortex but obtains a more circular shape as it grows. Figure 4.3 illustrates the pressure distribution along the sampling lines at different time steps. It can be seen that discrepancies between the location of the vortex centre and the minimum pressure do exist along the sampling line in the direction of $\theta = 0°$. In the initial state of the build-up the low pressure minimum is moved further out towards the corner from where the vortex originated. The discrepancy might be due to variation of velocity magnitude within the vortex. A higher velocity reduces the static pressure and would thereby extend the low pressure zone towards it and thereby move it. During the initial creation of the vortex the velocity on the free stream side of the vortex is of the same magnitude as the free stream fluid and the fluid on the other side is much lower.

Equation (4.2) describes the transport of momentum in a Cartesian frame of reference. Since the vorticies are characterised by a circular motion this will make an analysis of the transport of momentum difficult to interpret inside the vorticies. Some of the terms in equation (4.2) will most probably influences the flow differently in different part of the vortex. The pressure term would for example help to reduce and accelerate the flow in regions were protrusions exist, giving it a major influence on the velocity magnitude. With a perfectly circular topology with the low pressure minimum located in the vortex centre it would instead only redirect the flow and not influence the velocity magnitude. In order to get a better understanding of the terms influence on the flow an investigation from a different point of view would be more helpful. The velocity magnitude, static pressure and radial velocity distributions have been investigated in a cylindrical frame of reference, which would be more suitable for a circular flow. But neither that gives a clear division of the different terms effect in terms acceleration/retardation and redirection of the flow as both Figure 4.1 and 4.4 indicates distortions in the vortex topology. Instead the components in the momentum equation will be projected onto the normalised velocity vector, giving their influence on the velocity magnitude. The terms are in this way expressed as their

magnitude in the tangential direction of the flow, which for an arbitrary term in the momentum equation gives

$$M_t = \mathbf{M} \cdot \frac{\mathbf{u}}{|\mathbf{u}|} \tag{4.4}$$

A similar transformation for the part of the terms that redirects the flow is more difficult to develop. Since the direction of rotation can be arbitrary the transformation onto a vector orthogonal to the normalised velocity vector must be able to give consistent results in terms of inward or outward pointing contributions. To obtain the redirectional contribution are first the magnitude of the part orthogonal to the velocity vector computed, denoted m_o. It is then multiplied by the sign of the normalised radial part of the term. The radial part is obtained by projecting the terms vector onto a normalised position vector, $\hat{\mathbf{X}}/|\hat{\mathbf{X}}|$. $\hat{\mathbf{X}}$ is the position vector in a Cartesian coordinate system, located in the centre of the vortex, oriented in the same direction as the global coordinate system. The terms redirectional contribution, M_o, is then obtained. It is positive in the outward direction and are computed as in the equations below.

$$\begin{gathered} m_o = \sqrt{|\mathbf{M}|^2 - M_t^2} \\ M_r = \mathbf{M} \cdot \frac{\hat{\mathbf{X}}}{|\hat{\mathbf{X}}|} \qquad \hat{\mathbf{X}} = \mathbf{X} - \mathbf{X}_{vortex} \\ M_o = m_o \frac{M_r}{\sqrt{M_r^2}} \end{gathered} \tag{4.5}$$

The size of the vortex is increased during the build-up and when it is released the entire vortex moves downstream. During both parts of the process the centre of the vortex moves and accelerates downstream, indicating an imbalance of the forces acting on the fluid within the vortex. The effect can be seen in Figure 4.10, which illustrates the recovery of the time averaged streamwise velocity for geometry 4F for the unsteady RANS. Close to the cylinder the acceleration is large, further downstream it is reduced and at approximately 5 diameters from the cylinder centre the velocity appear to reach a steady value. The velocity recovery for the steady RANS is as expected much lower as indicated by Table 4.2. The velocity development of the vortex, and as a result the mean field, is determined by three processes. Figure 4.5 and 4.6 summarises the variation of the tangential and orthogonal parts of the terms in the momentum equation and together with the discussion and Figures presented above it gives an indication to the physics behind the development of the vortex. The terms have been evaluated along both the same sampling lines and at the same time steps as the velocity magnitude, static pressure and radial velocity presented above. It turns out that the flow is mainly dominated by the convection and the pressure terms, which are significantly larger than the contribution from the diffusion term. The convection and pressure terms have almost always a similar magnitude but with different signs. This is especially true for the orthogonal part whose total change of momentum, the Rate of change term, is of comparable size to that of the tangent equivalent even tough the magnitudes for the orthogonal terms is almost twice as large compared to the tangent in certain locations. Even tough the contribution from the diffusion term is much smaller due to the close relation between the convection and the pressure terms the influence from the diffusion becomes significant in the development of the vortex.

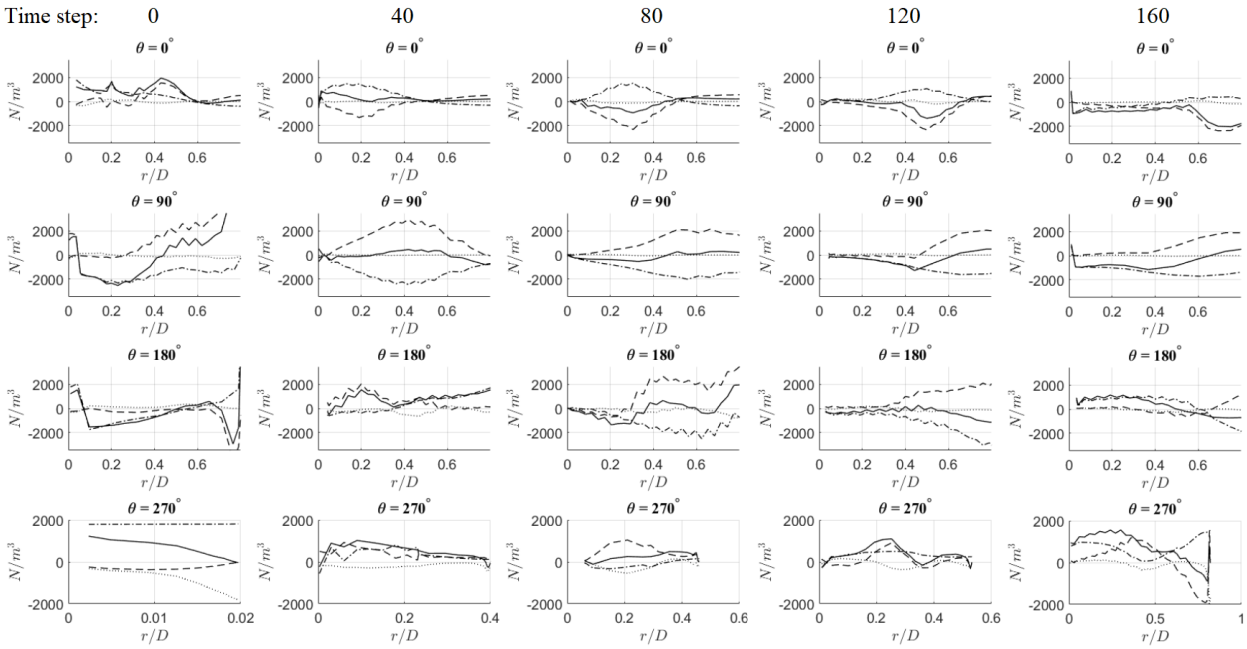

Figure 4.5: *Development of the tangential part, defined by equation* (4.4)*, of the terms in the momentum equation. From left to right is time step:* 0*,* 40*,* 80*,* 120 *&* 160*. Solid line: Rate of change, Dashed line: Convection, Dashed/Dotted: Pressure, Dotted: Diffusion.*

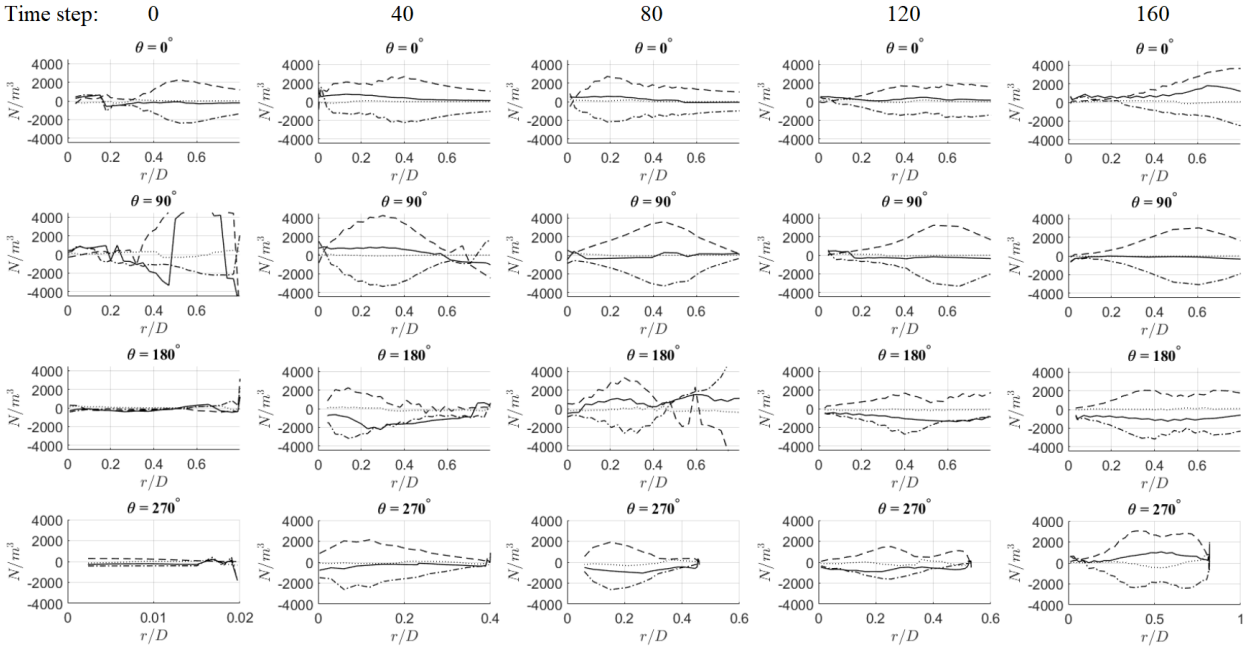

Figure 4.6: *Development of the orthogonal part, defined by equation* (4.5)*, of the terms in the momentum equation. From left to right is time step:* 0*,* 40*,* 80*,* 120 *&* 160*. Solid line: Rate of change, Dashed line: Convection, Dashed/Dotted: Pressure, Dotted: Diffusion.*

4.0.5 Summary of vortex development

The first part of the development of a vortex is the build-up, during which a vortex is created and amplified. The build-up can itself be divided into two phases. Common for the two phases is that they are both characterised by accumulation of mass and momentum, i.e increasing size and velocity. However, the development appears to change behaviour during the build-up. The initial creation of a vortex is induced by the movement of fluid from one of the separation bubbles on the side of the cylinders into the wake of the cylinder due to a low pressure, which creates a small separation around the corner. As seen in Figure 4.2 the flow that is being brought into the near wake, at $\theta = 0°$ and $90°$ at $r/D \approx 0.4$, has a rather high velocity comparable to that of the free stream fluid. Close to the streamline centre, at $r/D \approx 0.1$ which is the approximate size of the vortex at the 0^{th} time step, the velocity is much lower. The higher velocity further out gives a decreased static pressure, which as a result mean that the streamline centre and pressure minimum are not co-located. The low pressure region is moved in the downstream direction. The pressure distribution for the 0^{th} time step in Figure 4.3, at $\theta = 90°$ close to the centre, indicates that the minimum pressure is located at $r/D \approx 0.15$. Figure 4.6 further confirms that they are not co-located. At the same time step and for the same sampling line the orthogonal rate of change term is positive due to a positive pressure term, indicating a force in the down stream direction created by a decrease in pressure.The pressure term becomes zero at $r/D \approx 0.15$, indicating a pressure minimum. The fact that the pressure minimum is located downstream of the vortex centre results in a majority of the vortex being effected by a positive force in the streamwise direction. This gives the rapid increase in streamwise size seen in Figure 4.2 at the sampling line $\theta = 270°$. As the vortex grows, Figure 4.1 and 4.2 illustrates that the shape of the vortex becomes more circular and the distribution of velocity more even. At the 40^{th} time step in Figure 4.3 it can be observed that this results in a movement of the pressure minimum along $\theta = 90°$ toward the vortex centre. This reduces the streamwise growth rate, which is illustrated by the steady streamwise size observed in Figure 4.2 at $\theta = 270°$ around the 80^{th} time step.

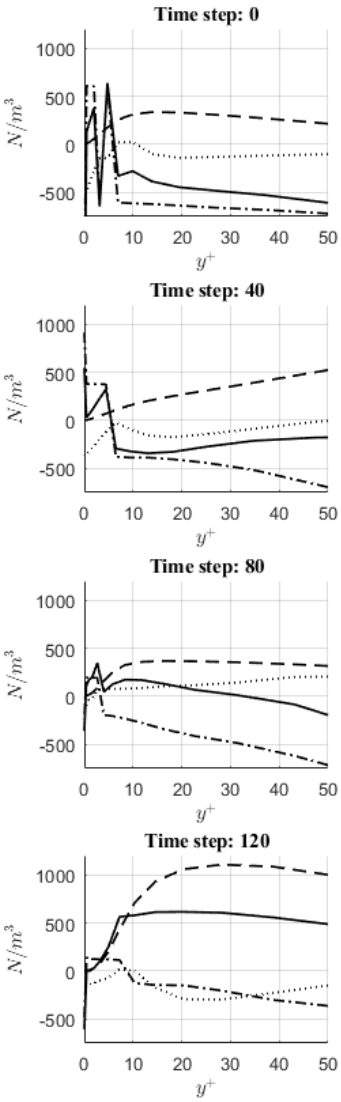

Figure 4.7: *Variation of the orthogonal terms in the momentum equation along the sampling line at $\theta = 270°$. A positive value represents a force upstream toward the cylinder. Close to the cylinder, within $y^+ < 5$, the pressure term is positive indicating a low pressure zone along the surface. Solid line: Rate of change, Dashed line: Convection, Dashed/Dotted: Pressure, Dotted: Diffusion.*

When the vortex has been established and obtained a more circular shape, the rapid streamwise growth is reduced. The build-up enters the second phase in which the vortex keeps growing and accumulating both mass and momentum. However, this phase is slower than the initial one. The velocity increases and the pressure decreases, but only slightly. The vortex has already been established during the initial phase, giving it both a more stable size and distribution of quantities. Maybe the largest change of the vortex can be seen in Figure 4.1. Even if the streamwise growth has slowed down, the vortex keeps growing. Instead the growth appears to be focused to the transverse direction giving the vortex a more round and full appearance. When the size of the vortex finally reaches a size comparable to the cylinder it is released from the surface. At this stage the fluid within the vortex is moved so far out towards the corner opposite from where it was created that it can interact with the free stream fluid on the other side of the cylinder. This enables the free stream fluid to enter the region between the vortex and the cylinder, which divides them and initiates the release of the vortex.

To summarise the build-up of the vortex the first phase establishes the vortex. During this phase the majority of the mass and momentum exchange between the free stream fluid and the base region takes place. This phase is enabled by a non co-located vortex centre and pressure minimum. It is ended when the vortex obtains a more circular shape, which moves the pressure minimum towards the vortex centre. When this phase

has ended the size of the vortex might not permit interaction with the free stream fluid on the other side of the cylinder. The second phase saturates the vortex by increasing its transverse size, which enables the free stream interaction and as a consequence the release of the vortex.

A clear division between the two phases are difficult to define. The changes appears to be rather gradual and might overlap. However, a number of impotant aspects for the development of the vortex can still be identified. The majority of the accumulation of mass and momentum takes place during the time that the vortex sticks to the cylinder surface. To obtain high accuracy it is therefore important to understand what is causing the vortex to stick to surface and what is causing the vortex to be released to be able to use the correct numerical setup.

As already stated the diffusion term has a marginal influence on the transport of momentum. However, the boundary layer at the back side of the cylinder gives high velocity gradients resulting in a much higher contribution, comparable to those of the other terms. Figure 4.7 illustrates the variation of the orthogonal rate of change, convection, pressure and diffusion term along the back surface of the cylinder. Both the rate of change and pressure term are positive closest to the wall, indicating that the force is created by a low pressure zone in the viscous sub-layer. The diffusion term is always negative close to the wall which means that it generates a force that wants to release the vortex from the cylinder surface. Further out a second minimum in the diffusion term can be observed. The inner one is due to the viscous forces in the viscous sub-layer. The minimum in the buffer layer and the inner part of the log-layer is due to the turbulent diffusion. Physically it makes sense that the diffusion term creates a force directed away from the wall. The thickness of the boundary layer grows as the fluid in the boundary layer is slowed down. The fast moving fluid further out is due to this growth pushed further away from the wall. In the viscous sub layer the magnitude of the pressure term is larger than the diffusion term causing a force towards the surface. In the buffer layer and log-law layer the magnitude of the convection term increases and the sign of the rate of change term is determined by the ration between the pressure and convection term.

In Figure 4.7 it can be observed that the rate of change term stays positive in the inner most part of the viscous sub-layer even if the vortex is being released at the 80^{th} time step. The release of the vortex is therefore not due to the rate of change term changing sign. Instead it is due to free stream fluid entering the region between the wall and the vortex resulting from a combination of the interaction between the free stream fluid and the fluid within the vortex and the low pressure found in the base region. The positive force then acts on the free stream fluid rather than the fluid contained within the vortex. A direct relation between the release of the vortex and the modelling of the turbulence can therefore not be made. However, the release of the vortex will be dependent on the sign of the rate of change term further out from the wall, a factor that is dependent on the turbulent diffusion. Since the turbulent diffusion term is negative and has a magnitude comparable to the other term it will have a significant contribution to how fast the release of the vortex is.

The flow around the cylinder will be two-dimensional for results obtained using RANS. The velocity and all velocity gradients in the span wise direction of the cylinder will therefore be zero. The velocity at the back surface of the cylinder along $\theta = 270°$ can be assumed to be parallel to the wall and directed in the negative y-direction inside the vortex. Therefore it is relevant to look at the transport equation for momentum in the Cartesian framework ones again to investigate the validity of the behaviour. From equation (2.6) and (2.10) we get the turbulent diffusion as

$$D_{i,turbulent} = \frac{\partial}{\partial x_j}\left(\mu_t\left(\frac{\partial\langle u_i\rangle}{\partial x_j} + \frac{\partial\langle u_j\rangle}{\partial x_i}\right)\right)$$

In this case can the velocity and its gradient in the span wise direction (z-direction) be assumed to be zero. The equation is then reduced to

$$D_{1,turbulent} = \frac{\partial}{\partial x_1}\left(\frac{\partial\langle u_1\rangle}{\partial x_1}\mu_t + \frac{\partial\langle u_1\rangle}{\partial x_1}\mu_t\right) + \frac{\partial}{\partial x_2}\left(\frac{\partial\langle u_1\rangle}{\partial x_2}\mu_t + \frac{\partial\langle u_2\rangle}{\partial x_1}\mu_t\right)$$

The velocity in the wall normal direction, u_1, will be damped by the wall and the terms in which it is including will therefore be small. By removing them remains only one term.

$$D_{1,turbulent} \approx \frac{\partial}{\partial x_2}\left(\frac{\partial\langle u_2\rangle}{\partial x_1}\mu_t\right)$$

The diffusion term will therefore be dependent on the modelling of the turbulence and the eddy viscosity. For $k-\omega$ SST the eddy viscosity is defined according to equation (2.13) as $\mu_t = \rho C_\mu k^2/\epsilon$. A higher turbulent kinetic energy, k, or a lower dissipation rate, ϵ, should give a lower rate of change term.

The release of the vortex is therefore somewhat connected to the turbulence, where an overestimated level of modelled turbulent kinetic energy should promote a quicker release of the vortex. This would effect the duration of time it sticks to the surface. It could also have an effect on the shape of the vortex, which from the discussion above seems to have a large effect on the growth of the vortex in its initial phase. Similar to the diffusion terms promotion of a fast release, the shape of the vortex would effect the accumulation rate of mass and momentum during the build-up and as a result could effect the time duration from the creation to the release of a vortex. Both of these effects can therefore have an influence on the predicted shedding frequency. The Strouhal number can be interpreted as the shedding frequency in relation to the amount of fluid passing by. Since the growth of the vortex and as a result the velocity recovery in the wake is related to the amount of momentum brought into the wake the Strouhal number would be of great importance. For a given cylinder diameter and free stream velocity and assuming a constant size of the saturated vortices a higher shedding frequency, and by definition a higher Strouhal number, mean that a larger amount of free stream fluid and momentum is brought into the wake. A higher transport of momentum into the wake would decrease the recirculation region length. The results presented in Table 4.3 seem to support that such a relation between the Strouhal number and recirculation region length exists. The lengths are consistently under predicted while the Strouhal number are over predicted.

The modelled k equation in eddy viscosity models has a number of known shortcomings. Bradshaw [3] and Rodi et al. [24] showed that convex streamlines, in which the velocity magnitude increases with the radius of the curved streamline, stabilises turbulence. Excluding the diffusion it can be shown from the momentum equation in cylindrical coordinates, in equation (4.6), that an increased velocity magnitude increases the pressure gradient.

$$\rho\frac{v_\theta^2}{r} = \frac{\partial P}{\partial r} \tag{4.6}$$

The pressure gradient is balanced by the centrifugal forces created by the curvature of the flow. If the velocity increases with the radius this gives an increasing pressure gradient with increased radius, i.e a greater forces toward the centre of the curved streamline. If a fluid element is moved outwards it will be effected by a larger force inward and since the velocity is lower at a smaller radius the centrifugal force will not balance the increased force from the pressure gradient. The movement is therefore counteracted. A movement inward would instead cause a higher centrifugal force which also counteracts the movement. If the velocity magnitude instead decreases with increased radius the pressure gradient would also decrease. A movement in the radial direction would in this case instead be reinforce by the pressure gradient, causing an unstable flow which promotes production of turbulence. Different turbulence models handles this flow situation differently. In the Reynolds Stress Model, which solves transport equations for each component in the Reynolds stress tensor, the production terms are connected and depends on the other stress components and an increase (or decrease) of one of the components due to curvature causes a feedback loop which increases (or decreases) all components. Eddy-viscosity models that uses the modelled k equation lacks this ability. The turbulent production is modelled as a linear relation between the eddy viscosity and the strain rate tensor which means that the same feed back loop does not exist. The current flow situation does contain curved streamlines, especially in the vortex itself. As illustrated by both Figure 4.2 and 4.3 the velocity magnitude increases with the radius in the vortex, which causes a larger pressure gradient in the outskirts of the vortex. This mean that the flow is stabilised. An eddy viscosity model might miss the dampening effect and over predict the turbulence, which as stated above would effect the growth and shape of the vorticies.

Another shortcoming of the modelled k equation is overproduction of turbulent kinetic energy in regions with stagnation flow[4]. The geometry 4F has a number of regions with this kind of flow. The most obvious is the front surface of the cylinder where the flow approaches the surface in the wall normal direction. Then there are more subtle regions with stagnation flows which are easily overseen. Both on the side of the cylinder and on the back surface stagnation flow is obtained when the separated flow reattaches. The fluid moves along the interface between the separated region and the free stream. As the flow approaches the wall the fluid within the separated zone is moved back into the separated region and the fluid outside it toward the other direction. The Reynolds stresses are related to k trough Bossinesqs assumption. Stagnation flows creates large velocity gradients, $\frac{\partial\langle u_1\rangle}{\partial x_1}$ and $\frac{\partial\langle u_2\rangle}{\partial x_2}$ assuming the flow is 2-dimensional in the xy-plane, which through the continuity gets opposite signs. The production of k in the modelled k equation is defined as

$$P^k = 2\mu_t S_{ij} S_{ij}$$

Because of $S_{ij}S_{ij}$ the production will not be dependent on the gradients directed but instead the square of the gradients. The different signs of $\frac{\partial u_1}{\partial x_1}$ and $\frac{\partial u_2}{\partial x_2}$ will not be recognised and they will both give a positive contribution. In RSM can the production of turbulent kinetic energy be written as

$$P^k_{rsm} = 0.5\big(P_{11} + P_{22}\big) = -\frac{\partial \langle u_1 \rangle}{\partial x_1}\left(\langle u_1'^2 \rangle^2 - \langle u_2'^2 \rangle^2\right)$$

The RSM production of k does not contain squared gradients and will therefore not over predict the production as the eddy viscosity model do. Table 4.3 indicates that RSM predicts a slightly longer recirculation region length, which might be due to a more accurate prediction of the turbulence.

The second part of the vortex life, or third if the two phases of the build-up is considered as two separate processes, is the dissolution and transport of the vortex downstream. As the vortex grows and mass and momentum is accumulated, it is observed in Figure 4.3 that the pressure is reduced. Both the reduction of the pressure and the increase of momentum, related to the build up of the vortex is reduced as the vortex is released. The increase in velocity magnitude is halted as soon as the vortex is released at around the 80^{th} time step. The pressure however keeps decreasing for some time and it is not until the 160^{th} time step that the pressure can be observed to increase. At this point both the pressure can be observed to increase and the velocity magnitude to decrease, a process which continues until the vortex is completely dissolved. As discussed above the distorted shape of the vortex seems to be related to the accumulation of fluid and momentum. When the influence of the low pressure zone in the viscous sub-layer keeping the vortex stuck to the surface is no longer effecting the vortex, it can obtain a more circular shape which reduces the transport of momentum into the vortex. The transport of momentum out of the vortex then takes over and the vortex is slowly dissolved. In Figure 4.5 it can be seen that the rate of change term is exclusively negative except for along the sampling line at $= 270°$. The diffusion also seems to increase slightly at $\theta = 180°$ where the velocity inside the vortex and the outside free stream velocity are directed in opposite directions. As seen in Figure 4.10 the velocity recovery of the mean field continues for a longer distance than can be covered by a vortex. A transport of momentum into the wake must therefore still be present. In Figure 4.2 it can be seen that the location at which the maximum velocity is observed changes when the vortex is released. During the build up the maximum velocity is found at $\theta = 0°$ and $90°$. As the vortex is released the velocity decreases in these regions. At $\theta = 270°$ the velocity continues to increase and due to this the position of maximum velocity magnitude is moved to this location. The terms investigated in Figure 4.5 seems to suggest that the only source of momentum after the release is found along the line in the $\theta = 270°$ direction where both the pressure and convection terms accelerates the flow.

4.0.6 Further improvement

Because of the fact that only an unsteady solver can capture the extra transport of momentum into the wake it can be concluded that steady RANS is unsuitable for these kinds of flows. The unsteady RANS has the potential of capturing the additional transport of momentum correctly and it gives somewhat reasonable, and especially consistent, results for the rather simple polygonal geometries investigated so far. From the discussion above it is reasonable to believe that the discrepancies between the experimental and numerical results are due to an excessive amount of numerical diffusion or that the investigated models are unable to capture these kind of flow with a high level of accuracy, even under perfect condition. Even if the discrepancy between the experimental results and that of the unsteady RANS are within an acceptable level for the polygonal case they are still not negligible in a more complex flow situation where the flow interact with several components along its path, which will result in accumulation of errors. Instead of implementing the methods into an engine bay the numerical setup will therefore be investigated further in order to either improve the accuracy and find the necessary requirements to obtain acceptable results or to be able to conclude that more advanced methods are a necessity.

The observed trends for each model and geometry are consistent for the unsteady RANS, indicating that the flows for all geometries are rather similar and constitutes similar challenges in terms of modelling. It is therefore not necessary to include all of them in a continued investigation. Because of this the set of shapes is reduced to only the geometry 4F. The reason for using 4F is that it has been the focus of an extensive amount of research, which gives a larger possibility to compare the obtained results with other studies than for the other geometries.

Even if some differences exist between the experiments and numerical results it does appear as if all models predicts the separation point rather well. It is possible that the reduced spectrum of possible separation points created by the polygonal shapes compared to a smoother shape reduces the differences in separation behaviour for the models. In order to investigate this further is a circular cross section added along geometry 4F. For a circular cross section the separation point can be more arbitrate than for the polygonal geometries and might be more challenging to predict. The flow past a cylinder with cylindrical cross section has, just like that of square cross sections, been studied extensively.

In order to reduce the computational cost the computational domain is reduced to create a geometry identical to that used for the LES and DES computations. The mesh strategy is changed from the local volume refinements used for the polygonal case to the same strategy used for the scale resolving methods, where the cell sizes are related to the large turbulent length scales. Prior to the computations a second mesh study was performed with this new method. The study was performed on the cylindrical geometry which was believed to constitute a larger challenge due to the more arbitrary separation point. Two mesh parameters were investigated, the surface cell size, Δx_s, and the number of cells per large scale eddy, n_c. The large turbulent length scales was computed as for the scale resolving methods by equation (3.2) in which the mean turbulent quantities were obtained using $k-\omega$ SST. The mesh for this computation was obtained using a similar mesh strategy as for the polygonal case, but with the medium and fine refinement boxes extended to the outlet. The cylinder refinement was removed and instead the cell sizes were adjusted to 60, 30 and 15% of the base size for the coarse, medium and fine refinement boxes respectively. The surface cell size was optimised first since it was found that the results showed little to no variation if the surface was incorrectly resolved when varying n_c. To limit the numerical diffusion and its possible effects on the separation during the first part of the study n_c is kept constant at 8. The surface cell size is varied between $\frac{\Delta x_s}{D} = 0.008$ and 0.072, where the larger value is slightly larger then that used for the polygonal geometries.

Figure 4.8 summarises the results obtained from the mesh study. The results are normalised with the results obtained from the finest mesh resolution. Both the characteristic lengths of the wake and the drag on the cylinder was investigated. It appears that the wake width and the drag on the cylinder are rather insensitive towards the surface cell size with a surface resolution below $\frac{\Delta x_s}{D} = 0.06$ with variations of only a few percent. The recirculation region length is more sensitive and it is not until $\frac{\Delta x_s}{D} = 0.03$ that the difference is below 5%. Even at $\frac{\Delta x_s}{D} = 0.02$ significant change can be seen which might indicate that an even finer mesh would be required. The results obtained with the finest resolution required a drastic reduction in time step size ($\Delta t U_\infty / D$) in order to limit the CFL number to obtain physical results. However, the results obtained with this resolution seems to deviate rather drastically from the consistent trend seen for the other resolutions. It is therefore possible that there still is some problems with this result. Due to drastic increase of the required computational power as the surface resolution is reduced below $\frac{\Delta x_s}{D} = 0.01$ a further refinement is not possible. The best possible results can therefore be obtained with a surface resolution of $\frac{\Delta x_s}{D} = 0.016$.

By investigating the skin friction coefficient the separation point can be identified. Figure 4.8 illustrates the variation of the separation point as the surface cell size is reduced. The separation angle is defined as the angle between the incoming free stream flow and the cylinder surface tangent at the separation point. As the mesh is refined the separation point moves upstream. The small discrepancies is most likely due to the restricted resolution given by the mesh, which varies between 0.92° and 8.25° between the cells. The later separation for the coarser meshes is most likely due to numerical diffusion, which just as turbulence provides the boundary layer with increased momentum.

The mesh study for the number of cells per large turbulent scale was performed with $\frac{\Delta x_s}{D} = 0.016$ and n_c was varied between 4 and 10. The parameters converges consistently toward a steady value and already at $n_c = 6$ is the difference rather small. A small change in the values is present even between the two finest meshes, which indicate that meshes still are not entirely mesh independent. The difference is however so small that the discrepancies can be neglected. A mesh with $n_c = 8$ is considered good enough for further investigation.

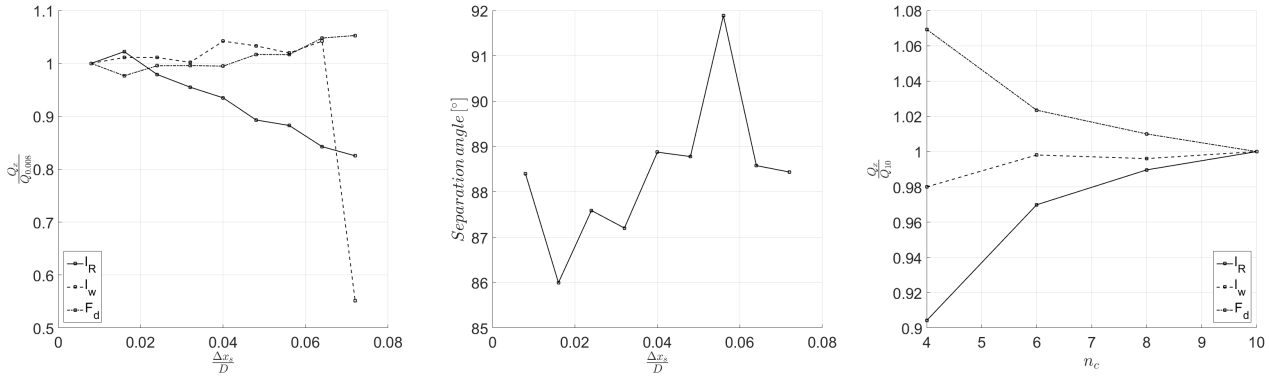

Figure 4.8: *Results for the mesh study obtained from the circular cross section with $k-\omega$ SST. The results for the characteristic lengths of the wake and the drag on the cylinder are all normalised by the results from the finest mesh resolution, $\frac{\Delta x_s}{D} = 0.008$ and $n_c = 10$. The mesh study of the surface resolution was performed first and with $n_c = 8$. The mesh study of n_c was then performed with $\frac{\Delta x_s}{D} = 0.016$.*

Table 4.4: Results for the circular and square geometry using unsteady RANS, DES & LES at $Re_d = 1 \cdot 10^4$ & $Re_d = 2.2 \cdot 10^4$, respectively.

Geometry: Cylinder	$C_d/C_{d,exp} - 1$ [%]	$l_R/l_{R,exp} - 1$ [%]	$l_w/l_{w,exp} - 1$ [%]	$St/St_{exp} - 1$ [%]
$k-\omega$ SST	4.12	-35.18	-4.42	0.38
$k-\epsilon$ Realizable	-30.04	-33.87	-10.36	29.93
RSM elliptic blending	3.28	-35.71	-4.49	6.37
$k-\epsilon\ \overline{v_2'^2}f$	2.44	-34.86	-4.14	1.56
Spalart Allmaras	13.09	-47.34	-8.36	-1.87
$k-\omega$ SST (DES)	6.50	-29.90	-1.63	-5.37
Smagorinsky model (LES)	-29.51	-19.21	-5.22	-20.36
Experiments by Xu et al. [30]	$C_{d,exp} = 1.105$	$l_{R,exp} = 2.050$	$l_{w,exp} = 1.150$	$St_{exp} = 0.205$

Geometry: 4F	$C_d/C_{d,exp} - 1$ [%]	$l_R/l_{R,exp} - 1$ [%]	l_w [%]	$St/St_{exp} - 1$ [%]
$k-\omega$ SST	3.00	-3.09	$1.58D$	-16.18
$k-\epsilon$ Realizable	2.36	-6.34	$1.54D$	-1.52
RSM elliptic blending	-5.83	26.25	$1.60D$	-3.72
$k-\epsilon\ \overline{v_2'^2}f$	-0.96	7.01	$1.56D$	-17.31
Spalart Allmaras	2.16	6.09	$1.63D$	-13.95
$k-\omega$ SST (DES)	-3.69	12.52	$1.61D$	0.50
Smagorinsky model (LES)	2.05	-16.99	$1.53D$	14.03
Previous studies (non-normalised)				
Experiments by Xu et al. [30]	$C_{d,exp} = 2.1(1.9-2.2)$	$l_{R,exp} = 1.38D$	-	$St_{exp} = 0.132$
Sohankar et al. [27] (Smagorinsky)	2.22	$1D$	-	0.127
Sohankar et al. [27] (D. Smagorinsky)	2.03	$1D$	-	0.126
Rodi [22] (Smagorinsky)	2.30	$1.46D$	-	0.130
Iaccariano et al. [11] ($k-\epsilon\ \overline{v_2'^2}f$)	2.22	$1.45D$	-	0.141
Elkhoury [9] (Spalart Allmaras)	2.13	$1.01D$	-	0.128

Table 4.4 summarises the results obtained for the square and circular cross sections. Compared to Table 4.3 a significant improvement can be observed for the square geometry, for which accurate results are obtained. The circular cross section however shows errors of similar magnitudes as for the polygonal cases. There might be a number of reasons for this. As already mentioned above a certain level of mesh dependence still exist. Bearman [2] found through experiments that the separation angle was close to 80° at $Re = 2 \cdot 10^4$. As the present results predicts a larger separation angle and a movement forward of the separation point as the surface cell size is reduced this would indicate that the accuracy of the results increases. The reason why the separation angle is overestimated is most likely due to a combination of overproduction of turbulent kinetic energy and numerical diffusion. It appears that in order to reduce the error in recirculation region length, scale resolving methods must be used.

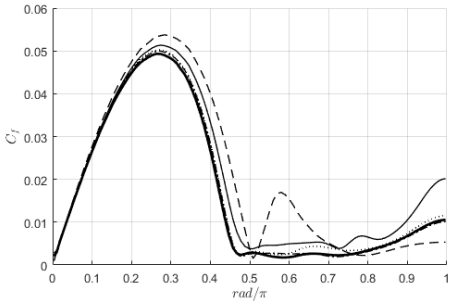

Figure 4.9: *Distribution of the skin friction coefficient long the surface of the cylinder. The angle is defined as the angle between the upstream edge of the circular cylinder and the tangent of the surface. Thick solid line: $k-\omega$ SST, Dashed line: $k-\epsilon$ Realizable, Dashed/Dotted line: RSM, Dotted line: $k-\epsilon$ V2F, Thin solid line: Spalart-Allmaras.*

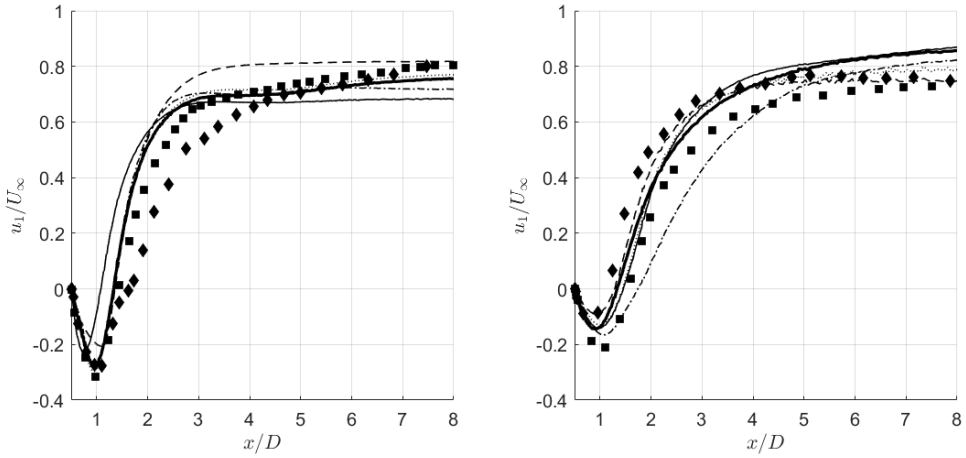

Figure 4.10: *Recovery of the streamwise velocity in the centre of the wake downstream of the cylinders. The circular cylinder is to the left and the square cylinder to the right. For legend see Figure 4.9.*

Figure 4.10 illustrates the recovery of the streamwise velocity. As already indicated in Table 4.4 the recirculation length predicted for the circular cross section by all of the URANS models and the DES are to small. The underestimated recirculation region lengths for all of the models are either due to the modelling of turbulence upstream of the separation point or the result of incorrectly predicted separation point. Figure 4.9 shows the skin friction coefficient along the surface of the cylinder. The separation point is defined at the point where the skin friction coefficient vanishes and reaches a minimum. From Figure 4.9 is it apparent that the predicted separation point varies little between the models. Figure 4.11 illustrates the mean of the total turbulent kinetic energy ($Modelled + Resolved$) along the centre line in the wake downstream of the cylinders. For the square geometry they appear to agree with the experimental results obtained by Lyn et al. [16]. The most obvious difference is between the circular and square geometry. For the circular cross section the turbulence is significantly lower for the LES results. For the square geometry the results from the RANS and scale resolving methods are in much better agreement. An overestimated turbulent kinetic energy can be observed also for the DES for the circular geometry. The only difference between the LES and DES is that DES uses URANS and $k\omega$ SST along the surface of the cylinder. As discussed earlier curved streamlines are one of the modelled k-equations weaknesses and the difference between the circular and square are that the circular geometry has curved surfaces. It is therefore likely that the larger errors seen for the circular geometry is due to the RANS models having problems to predict the turbulence correctly along curved surfaces.

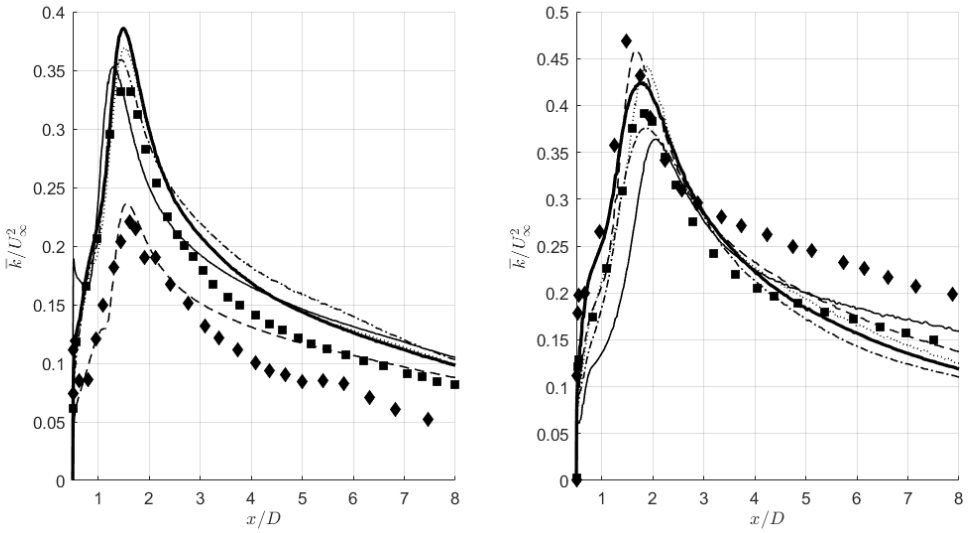

Figure 4.11: *Total turbulent kinetic energy (Modelled + Resolved) along the centre line in the wake downstream of the cylinders (upper row) and on the side of the cylinder at $x = 0$ (lower row) for the circular cylinder (left column) and the square cylinder (right column). The turbulent kinetic energies have been normalised by the free stream velocity. For legend see Figure 4.9.*

Figure 4.12a and 4.12b shows the normal Reynolds stresses in the centre of the wake downstream of the cylinders. The results for the square cylinder seems to agree rather well with both previous experimental performed by Lyn et al. [16] and numerical studies performed by Elkhoury [9] and Sohankar et al. [27] both when it comes to the magnitudes and the position of the maximum stresses. For the circular cross section a bit more variation in the results can be observed. For both the Reynolds stresses in the x- and z-direction are the position of the maximum stresses moved closer to the cylinder than for the scale resolving methods. The stresses in the y-direction are significantly over predicted.

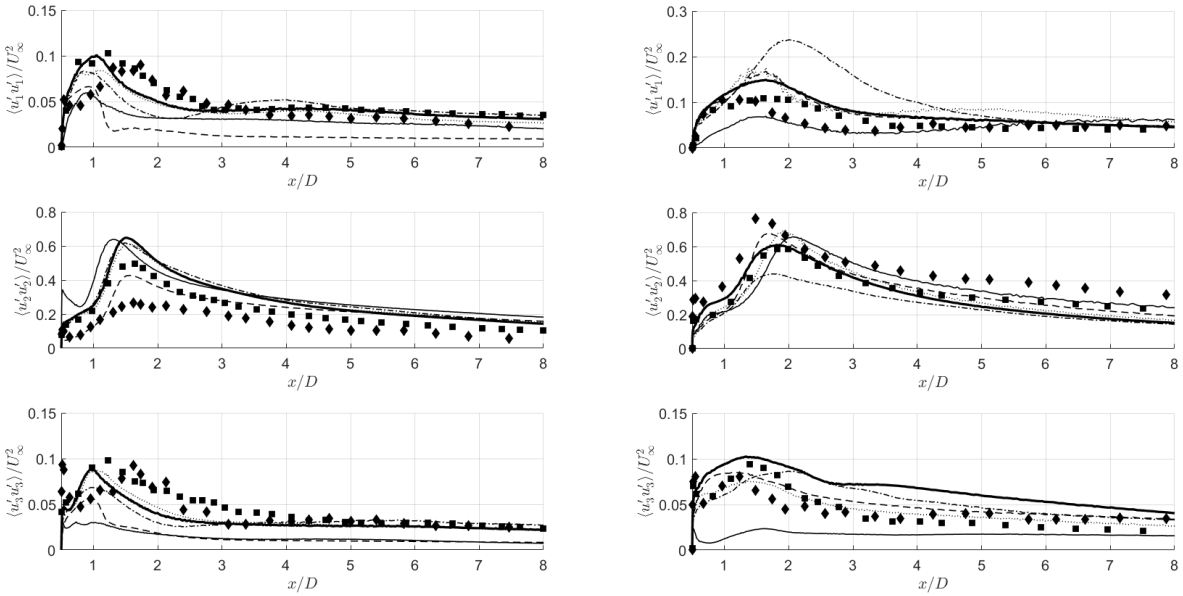

(a) (b)

Figure 4.12: *The normal components of the Reynolds stress tensor, which are normalised by the free stream velocity in the centre of the wake downstream of the cylinder. The circular cylinder is to the left and the square cylinder to the right. For legend see Figure 4.9.*

5 Conclusion

The unsteady flow around cylinders with different cross sections were investigated. The cross sections included a circular geometry and a number of polygonal shapes, with 2, 4, 7, 8 and 16 sides of different orientations. The investigation was performed at a Reynolds number of $Re_d = 1 \cdot 10^4$. The square geometry was also investigated at a Reynolds number of $Re_d = 2.2 \cdot 10^4$. Several Reynolds Averaged Navier-Stokes (RANS) models were investigated with both steady and unsteady solvers, including: $k - \omega$ SST, $k - \epsilon$ Realizable, Reynolds Stress Model, $k - \epsilon$ $\overline{v_2'^2} f$ and Spalart Allmaras. Detached Eddy Simulations (DES) using $k - \omega$ SST for the unsteady RANS part and Large Eddy Simulations (LES) using the Smagorinsky sub-grid model were also investigated.

It was found that separation and reattachment predicted by the different RANS models varied little, both for the steady and unsteady solver. For the polygonal shapes only a few errors were made. $k - \epsilon$ Realizable appeared to be slightly worse at predicting the separation point than the other models. For the circular shape the predicted separation points showed the same trend as for the polygonal shapes with small variations. Once again $k - \epsilon$ Realizble appeared to make larger errors and predicted the latest separation point. Common for both the polygonal shapes and the circle was that if the separation point were predicted incorrectly, the predicted separation point was located downstream compared to the separation point indicated by experiments performed by Xu et al. [30] and Bearman [2]. It is believed that this is due to numerical diffusion and an overestimated turbulent kinetic energy.

The largest difference between the steady and unsteady solver was the predicted recirculation region length in the time averaged velocity field downstream of the cylinder. The unsteady solver predicted a significantly shorter and more accurate recircualtion region length. The reason is the extra transport of momentum into the wake due to the vortex shedding process, which only a transient solver is able to resolve. It could therefore be concluded that the steady state solver was unsuitable for these kinds of flow.

The predicted creation and development of the vortices was investigated further for the square geometry using $k - \omega$ SST. It was found that the development of vortices can be divided into two different processes: A build-up process during which mass and momentum are accumulated to the vortices and a dissolvement process during which the accumulated momentum are removed from the vortex and spread to the surrounding fluid. The build-up could be further divided into two phases: One initial phase with rapid accumulation of mass and momentum and one second phase with slower accumulation of mass and momentum. During the initial phase the vortices are created and the streamwise size of the vortices are established. The rapid streamwise increase of the vortex size was due to a non co-located streamline centre and pressure minimum, where the low pressure minimum was located further downstream. During the second phase the transverse size of the vortices is increased, which eventually ends when the vortices have a size comparable to the cylinder. At that time the vortex starts to interact with the free stream fluid on the other side of the cylinder. Partially due to the free stream interaction and a decreased pressure within the vortices is free stream fluid pulled into the region between the cylinder and the vortex. This eventually results in the release of the vortex.

The vortices sticks to the surface of the cylinder during the build up. The behaviour was found to be the result of a low pressure zone within the inner most part of the viscous sub-layer. This force is preserved during the entire build-up, release and dissolvement of the vortices. The release of the vortices are instead caused by the free stream fluid moving the fluid within the vortices further out from the wall into the buffer and log-layer where the turbulent diffusion and pressure term in the momentum equation results in a downstream pointing force. Because of this the modelling of the eddy viscosity in eddy viscosity models have a certain influence on the release rate of the vortices, where an overestimated eddy viscosity seems to promote a faster release. For the eddy viscosity models which solves the modelled k-equation this means that an overestimated turbulent kinetic energy promotes a faster release.

The vortex shedding process can be predicted with adequate accuracy with the simple URANS models for polygonal shapes if the temporal and spacial resolution are fine enough. The circular cross section proved to be a greater challenge and results with non negligible errors was obtained in the form of underestimated recirculation region lengths. The reason was believed to be an overproduction of turbulent kinetic energy.

5.1 Future work

Due to the demand for both high spacial and, most importantly, temporal resolution URANS is considered unsuitable for implementation in complete engine bay situations in its current form. Neither the accuracy nor the computational power needed to obtain stable mean fields are the reason. To obtain stable mean fields, only a few vortex shedding cycles are required. The reason is that the thermal situation within the engine bay needs significant amount of time, in order of 30 minutes in order to stabilise, a simulation time that makes the computations to computationally heavy. The implementation is therefore somewhat dependent on how much the required computational resources can be reduced.

An uncertainty in the present study is the required surface mesh resolution for the circular geometry. For the present work the surface cell size was restricted to $\frac{\Delta x_s}{D} = 0.016$ due to the drastic increase of the cell count and required computational power below this point. However, the results from the mesh study indicated that the separation point had not reached a steady value, which means that a mesh dependence is still present. An investigation of the required surface cell size is needed for a number of reasons. The first is to see if the investigated models are able to predict the location of the separation point correctly even at ideal conditions. It is already known that eddy viscosity models creates an overproduction of turbulent kinetic energy. In the present study it has also been shown that this behaviour is increased by curved surfaces. The second reason is to reduce the computational cost when the findings are implemented in a detailed engine bay. Even for the simple geometries investigated in this study has the cell count proved to be a limiting factor, which means that it would most probably not be feasible using the same resolution in an engine bay. An investigation if a local refinement at the separation point is enough or if the hole surface up stream of the separation has to be resolved could therefore save a lot of time and computational power.

References

[1] W. Balzer and H. Fasel. Numerical investigation of the role of free-stream turbulence in boundary-layer separation. *Journal of Fluid Mechanics* **801** (2016), 289–321.

[2] P. Bearman. On vortex shedding from a circular cylinder in the critical Reynolds number regime. *Journal of Fluid Mechanics* **37**.3 (1969), 577–585.

[3] P. Bradshaw. *Effects of streamline curvature on turbulent flow.* Tech. rep. ADVISORY GROUP FOR AEROSPACE RESEARCH and DEVELOPMENT PARIS (FRANCE), 1973.

[4] L. Davidson. *Fluid mechanics, turbulent flow and turbulence modeling.* 2015.

[5] L. Davidson. "How to estimate the resolution of an LES of recirculating flow". *Quality and Reliability of Large-Eddy Simulations II.* Springer, 2011, pp. 269–286.

[6] L. Davidson. Large eddy simulations: how to evaluate resolution. *International Journal of Heat and Fluid Flow* **30**.5 (2009), 1016–1025.

[7] L. Davidson, P. V. Nielsen, and A. Sveningsson. Modifications of the $\overline{v_2'^2} - f$ model for computing the flow in a 3D wall jet (2003).

[8] P. Durbin. On the k-ε stagnation point anomaly. *Int. J. Heat and Fluid Flow* **17** (1996), 9–90.

[9] M. Elkhoury. Assessment of turbulence models for the simulation of turbulent flows past bluff bodies. *Journal of Wind Engineering and Industrial Aerodynamics* **154** (2016), 10–20.

[10] P. Gullberg. *Optimisation of the flow process in engine bays-3d modelling of cooling airflow.* Chalmers University of Technology, 2011.

[11] G. Iaccarino et al. Reynolds averaged simulation of unsteady separated flow. *International Journal of Heat and Fluid Flow* **24**.2 (2003), 147–156.

[12] T. Jongen. Simulation and modeling of turbulent incompressible fluid flows (1998).

[13] M. Khaled et al. Review of underhood aerothermal management: Towards vehicle simplified models. *Applied Thermal Engineering* **73**.1 (2014), 842–858.

[14] S. Lardeau and R. Manceau. "Computations of complex flow configurations using a modified elliptic-blending reynolds-stress model". *Proc. 10th ERCOFTAC Int. Symp. on Eng. Turb. Modelling and Measurements, Marbella, Spain.* 2014, p. 94.

[15] F. Lien, G. Kalitzin, and P. Durbin. RANS modeling for compressible and transitional flows. *Proceedings of the Stanford University Center for Turbulence Research Summer Program* (1998), 267–286.

[16] D. Lyn et al. A laser-Doppler velocimetry study of ensemble-averaged characteristics of the turbulent near wake of a square cylinder. *Journal of Fluid Mechanics* **304** (1995), 285–319.

[17] A. Menon. "NACA Ducts in vehicle thermal simulations". MA thesis. 2017.

[18] F. R. Menter. Improved Two-Equation k-εTurbulence Models for Aerodynamic Flows. *NASA Technical Memorandum* **103975** (1992).

[19] F. R. Menter. Two-equation eddy-viscosity turbulence models for engineering applications. *AIAA journal* **32**.8 (1994), 1598–1605.

[20] F. Menter and M. Kuntz. "Adaptation of eddy-viscosity turbulence models to unsteady separated flow behind vehicles". *The aerodynamics of heavy vehicles: trucks, buses, and trains.* Springer, 2004, pp. 339–352.

[21] A. Perry and T. Steiner. Large-scale vortex structures in turbulent wakes behind bluff bodies. Part 1. Vortex formation processes. *Journal of fluid mechanics* **174** (1987), 233–270.

[22] W. Rodi. Comparison of LES and RANS calculations of the flow around bluff bodies. *Journal of wind engineering and industrial aerodynamics* **69** (1997), 55–75.

[23] W. Rodi. "Experience with two-layer models combining the k-epsilon model with a one-equation model near the wall". *29th Aerospace sciences meeting.* 1991, p. 216.

[24] W. Rodi and G. Scheuerer. Calculation of curved shear layers with two-equation turbulence models. *The Physics of Fluids* **26**.6 (1983), 1422–1436.

[25] T.-H. Shih et al. A new k- eddy viscosity model for high reynolds number turbulent flows. *Computers & Fluids* **24**.3 (1995), 227–238.

[26] J. Smagorinsky. General circulation experiments with the primitive equations: I. The basic experiment. *Monthly weather review* **91**.3 (1963), 99–164.

[27] A. Sohankar, L. Davidson, and C. Norberg. Large eddy simulation of flow past a square cylinder: comparison of different subgrid scale models. *Journal of Fluids Engineering* **122**.1 (2000), 39–47.

[28] P. R. Spalart and C. L. Rumsey. Effective inflow conditions for turbulence models in aerodynamic calculations. *AIAA journal* **45**.10 (2007), 2544–2553.

[29] P. Spalart and S. Allmaras. "A one-equation turbulence model for aerodynamic flows". *30th aerospace sciences meeting and exhibit*. 1992, p. 439.

[30] S. Xu et al. Experimental study of flow around polygonal cylinders. *Journal of Fluid Mechanics* **812** (2017), 251–278.